

Copyright

by

Aaron Benjamin Morris

2009

**Investigation of a Discrete Velocity Monte Carlo Boltzmann Equation
Solver**

by

Aaron Benjamin Morris, B.S.

Thesis

Presented to the Faculty of the Graduate School of

The University of Texas at Austin

in Partial Fulfillment

of the Requirements

for the Degree of

Masters of Science in Engineering

The University of Texas at Austin

May 2009

Investigation of a Discrete Velocity Monte Carlo Boltzmann Equation Solver

**Approved by
Supervising Committee:**

Dedication

Dedicated to my parents.

Acknowledgements

I wish to express my gratitude to my advisors, Professor David Goldstein and Professor Philip Varghese for their continuing support and expert advice. I'd like to also thank them for the prompt and insightful feedback they have provided throughout this research. I'd also like to acknowledge funding for this research provided by NASA cooperative agreement NNX08AB27A under the EDL program, monitored by Technical Officer Robert Rubinstein.

4/30/09

Abstract

Investigation of a Discrete Velocity Monte Carlo Boltzmann Equation Solver

Aaron Benjamin Morris, MSE

The University of Texas at Austin, 2008

Supervisors: David Goldstein and Philip Varghese

A new discrete velocity scheme for solving the Boltzmann equation has been implemented for homogeneous relaxation and one-dimensional problems. Directly solving the Boltzmann equation is computationally expensive because in addition to working in physical space, the nonlinear collision integral must also be evaluated in a velocity space. To best solve the collision integral, collisions between each point in velocity space with all other points in velocity space must be considered, but this is very expensive. Motivated by the Direct Simulation Monte Carlo (DSMC) method, the computational costs in the present method are reduced by randomly sampling a set of collision partners for each point in velocity space. A collision partner selection algorithm was implemented to favor collision partners that contribute more to the collision integral. The new scheme has a built in flexibility, where the resolution in approximating the

collision integral can be adjusted by changing how many collision partners are sampled. The computational cost associated with evaluation of the collision integral is compared to the corresponding statistical error. Having a fixed set of velocities can artificially limit the collision outcomes by restricting post collision velocities to those that satisfy the conservation equations and lie precisely on the grid. A new velocity interpolation algorithm enables us to map velocities that do not lie on the grid to nearby grid points while preserving mass, momentum, and energy. This allows for arbitrary post-collision velocities that lie between grid points or completely outside of the velocity space to be projected back onto the nearby grid points. The present scheme is applied to homogeneous relaxation of the non-equilibrium Bobylev Krook-Wu distribution, and the numerical results agree well with the analytic solution. After verifying the proposed method for spatially homogeneous relaxation problems, the scheme was then used to solve a 1D traveling shock. The jump conditions across the shock match the Rankine-Hugoniot jump conditions. The internal shock wave structure was then compared to DSMC solutions, and good agreement was found for Mach numbers ranging from 1.2 to 6. Since a coarse velocity discretization is required for efficient calculation, the effects of different velocity grid resolutions are examined. Although using a relatively coarse approximation for the collision integral is computationally efficient, statistical noise pollutes the solution. The effects of using coarse and fine approximations for the collision integral are examined and it is found that by coarsely evaluating the collision integral, the computational time can be reduced by nearly two orders of magnitude while retaining relatively smooth macroscopic properties.

Table of Contents

List of Figures	x
CHAPTER 1: INTRODUCTION	1
Numerical Tests.....	5
CHAPTER 2: THEORY	7
Section 1: Velocity distribution Function.....	7
Scaling The Moments of The Distribution Function:.....	8
Section 2: The Boltzmann Equation.....	10
CHAPTER 3: METHOD	15
Section 1: Creating the Physical and Velocity Domains.....	15
Numerical integration:	16
Time Splitting Method.....	18
Section 2: Collisions.....	18
Depleting Collisions	19
Picking Collision Partners.....	20
Replenishing Collisions	22
Interpolation Scheme	24
Negative Mass	28
Section 3: Convection.....	30
Boundary Conditions	32
CHAPTER 4: NUMERICAL RESULTS	33
Section 1: Spatially Homogeneous Relaxation.....	33
Section 2: Different Grid Resolutions	44
Problem Statement.....	48
Numerical Results:	49
Velocity Grid Resolution	53

Internal Shock Structure	56
Cost Comparison	61
CHAPTER 5: CONCLUSIONS	65
Interpolation Scheme	65
Statistical evaluation of the Collision Integral	66
Homogeneous Results	66
1D Traveling Shock Results.....	67
Future Work.....	68
APPENDIX A: STATISTICAL EVALUATION OF THE DEPLETING INTEGRAL	69
REFERENCES	74
VITA	77

List of Figures

Figure 2.1.1. On the left side, a planar slice of a continuous velocity distribution is plotted. The right hand side is the delta function approximation to the continuous velocity distribution function.....	10
Figure 3.1.1. A discrete velocity distribution function represented by a set of delta functions.	17
Figure 3.2.1. A set of random collision partners M_j is chosen to collide with η_i . The selection of collision partners biases those that contribute more to the collision integral.....	20
Figure 3.2.2. A sample plot of the cumulative distribution function Ψ . Large steps correspond to large values of ϕ and smaller steps correspond to smaller values of ϕ	22
Figure 3.2.3. Collision circle drawn in 2D. Elastic collisions between η and ζ result in post collision velocities that lie on the black circle. The blue lines represent the pre-collision velocities and the green and red lines are post-collision velocities.	23
Figure 3.2.4. A 7-point symmetric stencil when the point to be interpolated lies within the cubic velocity domain.	24
Figure 3.2.5. A collision that results in a post collision velocity that lies outside of the domain.	26
Figure 3.2.6. A 5-point stencil (o, ix, iy, iz, ez) where the point to be interpolated lies outside of the velocity domain and is mapped back into the defined velocity space. The line connecting points iz and ez represent an edge of the velocity domain.	27

Figure 4.1.1 Instantaneous realizations of the Bobylev-Krook Wu distribution with a depleting fraction of 80% at three different times. For comparison are the corresponding GS solutions.	34
Figure 4.1.2. Instantaneous realizations of the BKW distribution with a depleting fraction of 40% at three different times.	35
Figure 4.1.3. Un-averaged instantaneous realizations of the BKW distribution with a depleting fraction of 5% at three different times.	36
Figure 4.1.4. The RMS difference between an un-averaged GS solution and ensemble averaged solutions generated with a 5% depleting fraction.	37
Figure 4.1.5. The entropy evolution for ensemble averaged solutions generated with a 5% depleting fraction compared to the N^2 solution.....	38
Figure 4.1.6. The entropy evolution without ensemble averaging for solutions generated with 40% and 80% depleting fractions.....	38
Figure 4.1.7. Slices of a Maxwellian distribution generated with different numbers of replenishing pairs.	39
Figure 4.1.8. Entropy evolution of a Maxwellian distribution for various numbers of replenishing pairs per collision.	40
Figure 4.1.9. RMS between the GS solution and solutions computed with various replenishing pairs per collision.	40
Figure 4.1.10. Rate of convergence by varying the depleting fraction and number of replenishing pairs.	42
Figure 4.1.11. Contour plot for a variable depleting fraction described by equation 4.1.3. CPU time is the time per collision step and is color contoured and the rms error in the distribution is contoured by lines.	43

Figure 4.2.1. Planar slices of the integrands in the zeroth and 2 nd moments of the Maxwellian distribution function. The velocity domain extends to ± 2.5	44
Figure 4.2.2. Planar slice of the 4 th moment of a Maxwellian distribution. The velocity domain extends to ± 2.5	45
Figure 4.2.3. Numerical integration errors in density, temperature, entropy, and the 4 th moment. The properties are scaled by the analytic values.	46
Figure 4.2.4. The error in entropy plotted for a relaxed distribution for various velocity spacings.	46
Figure 4.2.5. The error in the 4 th moment plotted for various grid spacings	47
Figure 4.3.1. 1D traveling shock schematic. The shock forms by reflection off the specular wall.	48
Figure 4.3.2. A schematic showing different parameters to quantify the internal shock structure.	49
Figure 4.3.3. Mach 1.97 shock profiles when the shock first forms ($\hat{t}=5$), when the shock is fully developed ($\hat{t}=100$), and an intermediate position ($\hat{t}=30$).	50
Figure 4.3.4. Snapshots of the scaled heat flux for a Mach 1.97 shock.	51
Figure 4.3.5. Slices of the distribution along the x-velocity axis downstream, upstream, and inside the shock. The symbols are the lattice sites. .	52
Figure 4.3.6. Mach 1.97 shock profiles generated with velocity grids of varying resolutions.	53
Figure 4.3.7. Mach 1.97 temperature profiles computed with velocity grids of varying resolutions.	54

Figure 4.3.8. Slices of the distribution function immediately ahead and downstream of a Mach 1.97 shock. The symbols correspond to lattice sites.	55
Figure 4.3.8. Mach 1.97 temperature profile obtained with a scaled velocity spacing of 1.0 and depleting fractions of 1% and 60%.....	56
Figure 4.3.9. Mach 1.97 shock profiles comparing discrete velocity solutions to DSMC solutions.....	57
Figure 4.3.10. Mach 1.2 shock profiles comparing discrete velocity and DSMC solutions.....	58
Figure 4.3.11. Mach 6.01 shock profiles comparing discrete velocity and DSMC solutions.....	60
Figure 4.4.1. Noise in the density upstream (squares) and downstream (triangles) of the shock wave plotted against the computational time for discrete velocity and DSMC solutions.....	63

CHAPTER 1: INTRODUCTION

It is well known that the Boltzmann equation can be used to describe non-equilibrium gas flows where the Navier-Stokes equations fail. Particular applications include problems such as satellite drag, flow within micro-devices, and solving for the internal shock structure. In each of these cases the mean free path is on the same order as the characteristic length scale for the problem.

Direct numerical simulation of the Boltzmann equation via a discrete velocity model can be used to describe a non-equilibrium gas flow, but computational costs limit its use. Hence, for flows that span the continuum to rarefied regimes, it would be more efficient to use a hybrid solver that restricts the computation of the non-equilibrium flow to the rarefied part where it is necessary, and uses the more efficient continuum solver where there is little error associated with its use. A low noise solution is required at the interface between the two because statistical fluctuations can contaminate the boundary conditions for the continuum calculations. This is a problem for the Direct Simulation Monte Carlo (DSMC) method [1], where instantaneous flow properties are subject to substantial statistical fluctuations, especially for transient problems. Statistical noise inherent to DSMC calculations is regarded as one of the major obstacles in developing a hybrid solver [2,3]. Since there is little statistical noise associated with the macroscopic flow variables in a direct solution of the Boltzmann equation via a discrete velocity model, such a method may be more efficient than the DSMC method, particularly for transient problems.

In a discrete velocity model, the infinite velocity space is truncated and discretized. Instead of having a continuum of velocities, a fixed set of discrete velocities approximate the velocity space. For most problems of interest, the combined phase space

will have at least 6 dimensions, three components for physical space and three for velocity space. If additional physics are specified, such as chemistry or internal energy, the dimensionality of the problem will be larger. This leads to very expensive calculations and consequently the velocity space must be limited to a relatively coarse discretization for efficient calculations.

In addition to discrete velocity methods, probabilistic Monte Carlo techniques have been used successfully for the full nonlinear Boltzmann equation. DSMC solves the Boltzmann equation by appealing to the physics of molecular interactions. DSMC has been applied to many problems with complex physics including chemically reacting flows with different internal energy modes. For near continuum flows DSMC can be inefficient because a large number of collisions need to be performed. Monte Carlo techniques can suffer from their statistical fluctuations because the error decay rate is of the order $N^{-1/2}$, where N is the number of computational particles. In order to obtain a smooth solution for an unsteady problem ensemble averaging may be used. It is expensive to ensemble average many transient simulations or produce a large single output simulation and consequently alternative ways of solving the Boltzmann equation are examined.

Discrete velocity methods have been used in schemes such as the Hicks-Yen-Nordsieck (HYN) method, [4,5]. Similar numerical strategies have been developed by Tcheremisine in [8]. In the HYN scheme, the collision integral is approximated by a Monte Carlo method. To approximate the collision integral, a mean value of the integral is computed by sampling a sufficiently large set of N values of the integrand. Since the collision integral is only approximated this scheme does not enforce mass, momentum, and energy conservation. Consequently, the HYN method requires a correction scheme to enforce conservation, but these corrections may limit the accuracy of the solution.

Alternatively, a discrete velocity model is exemplified by the Δ - ε model [6]. In this model, the collisions are performed by a Monte Carlo-like method. However, in this model and similar schemes discussed in [7,9], the post-collision velocities are restricted to those that lie on the grid. Although this scheme enforces conservation of mass, momentum, and energy the restricted set of grid-dependent post collision velocities can artificially reduce the collision integral when a coarse discretization is used in velocity space. Both the HYN method and the Δ - ε model can be applied to mixed continuum and rarefied flow problems but the computational costs are high, especially for high Mach number flows. For a high Mach number flow, the velocity space needs to be very large. Different regions of the flow can have vastly different bulk velocities, and simply coarsening the domain is not sufficient because the mesh size must be similar for both the low and high velocity regions. Consequently, many grid points are required and this leads to a high computational cost.

The Bhatnagar, Grook, and Krook (BGK) method, [11], can be readily implemented in a discrete velocity model where a linearized approximation for the collision integral is solved instead of computing the nonlinear collision integral. The BGK collision step drives a non-equilibrium distribution towards a Maxwellian distribution computed with the local kinetic temperature, velocity, and mass. The parameter to adjust the rate of relaxation has a somewhat arbitrary definition, where the rate of relaxation is proportional to the collision frequency. Using the BGK approximation for the collision integral does not guarantee the correct rate of relaxation. Instead it guarantees that the distribution function will relax to an equilibrium distribution. These errors can appear in solving for the shock structure because the shock structure heavily depends on the rate at which the gas equilibrates. The shock thickness becomes thinner as the gas equilibrates quicker.

The proposed discrete velocity scheme is a further development of previous work [12]. A portion of the present work was reported in [13]. Traditional discrete velocity Monte Carlo schemes can be limited by the restriction that post-collision velocities must lie on the grid and the associated large computational costs. The proposed scheme attempts to address both of these issues. For collision pairs with small relative velocities, there exist few post-collision velocities that lie on the grid. To overcome this problem, we pick an arbitrary orientation of the post-collision velocity vector and use the interpolation scheme to map those points back onto the grid. This interpolation routine precisely conserves mass, momentum, and energy and can be extended to points that lie entirely outside of the finite sub-set of velocity space that is used in the computation. Similar interpolation schemes were developed by Tcheremissine in [14-16] by splitting the post-collision component into two parts and accounting for them at two nearby nodes. The nodes to be interpolated to are selected such that the symmetry ensures that momentum is automatically conserved. An additional constraint is enforced such that the energy is conserved. Although conservative, this interpolation scheme is valid only for uniform velocity grids and does not readily accommodate post-collision velocities that lie outside of the velocity space. Other methods, e.g. [17], have generalized Tcheremissine's interpolation method to non-uniform grids but these schemes introduce slight errors in conservation of mass, momentum, and energy. To eliminate these errors, a correction scheme was implemented.

The nonlinear collision integral is responsible for most of the computational effort. Varghese showed that accurate evaluation of the replenishing integral can be obtained using a very coarse approximation, only replenishing to several pairs [12]. In this work the depleting integral was evaluated by considering collisions between each point in velocity space with every other point in velocity space. Since accurate results

were obtained using a coarse description of the replenishing integral, a coarser description of the depleting integral was also developed [13]. To coarsen evaluation of the depleting integral, collisions are performed between each point in velocity space with a representative set of partners that are chosen randomly. It was shown that accurate results could be obtained for significantly less computational effort by performing collisions with a representative set of partners instead of all possible collision partners. By varying how many collision partners are sampled, one can control how accurately to evaluate the collision integral depending on noise requirements. This scheme was then applied to a set of spatially homogeneous relaxation problems and now to a 1-D unsteady problem.

NUMERICAL TESTS

Exact solutions to the Boltzmann equation are rare. Since the major computational difficulty lies in evaluating the collision integral, a series of homogeneous relaxation tests are performed first. If a distribution that is initially Maxwellian is allowed to relax through collisions it should remain invariant because the Maxwellian distribution is the equilibrium distribution. This implies that all moments of the distribution should remain constant. Constancy of the first few moments indicate mass, momentum, and energy conservation. Conservation of higher moments reflect preservation of more subtle details of the distribution, especially the high velocity tails. These are minimum tests of a scheme. Note that the BGK approximation, for example, can pass these tests even though it is not an accurate solution to the collision integral for a non-equilibrium distribution. One particular example of an exact analytic solution to the time-dependent spatially homogeneous Boltzmann equation is for the Bobylev Krook Wu, *BKW*, distribution, [18,19]. Thus this solution can be used to assess how accurately the collision integral is calculated for an initial distribution that is far from equilibrium.

Once the homogeneous test cases were verified, the scheme was then applied to a moving 1D shock wave. 1D shock wave problems have commonly been used to test the validity of different numerical schemes, and shock wave profiles have been well documented for various intermolecular potentials [1,20,21]. To generate the shock wave, a gas initially moving to the left encounters a specular wall. A shock wave then propagates to the right, bringing the gas to rest while raising the temperature and density. Jump conditions are compared to the Rankine-Hugoniot conditions and the internal shock structure is compared to DSMC solutions. The characteristic parameters of the shock structure compared are the maximum-slope shock thickness measured on the density profile and the shift between the temperature and density profiles.

CHAPTER 2: THEORY

In the following chapter, a brief survey of the theory behind the velocity distribution function and Boltzmann equation is first presented before developing the numerical method used to solve the Boltzmann equation.

Section 1: Velocity distribution Function

From a molecular viewpoint, a gas is made up of many particles moving chaotically [22]. If the molecular diameter is small relative to the mean free path, then the gas is dilute. For a dilute gas, collisions are infrequent events that instantaneously change the velocity of a particle and most of the collisions are binary. Within a small volume, there exist N molecules traveling with different velocities. The velocity distribution function, φ , defines how many molecules inside of the small physical volume have a velocity between $\vec{\eta}$ and $\vec{\eta} + d\vec{\eta}$. If one scales φ by the local number density the resulting distribution, f , is the single particle velocity distribution function. This distribution defines the probability of a molecule having a velocity within $\vec{\eta}$ and $\vec{\eta} + d\vec{\eta}$. From this distribution, it is possible to compute all macroscopic variables of interest. The first three moment equations for number density, velocity, and temperature are:

$$n = \int_{\eta} \varphi dV_{\eta} \quad 2.1.1a$$

$$u_i = \frac{1}{n} \int_{\eta} \eta_i \varphi dV_{\eta} \quad 2.1.1b$$

$$T = \frac{m}{3k_B} \overline{C^2} = \frac{m}{3k_B n} \int_{\eta} (\eta_i - u_i)^2 \varphi dV_{\eta} \quad 2.1.1c$$

In addition to computing the density, momentum, and energy the distribution function also can be used to compute the heat flux, shear stress, and entropy.

$$q_j = \frac{1}{n} \int \frac{1}{2} m (\eta_j - u_j) (\eta_i - u_i)^2 \phi dV_\eta \quad 2.1.1d$$

$$\tau_{ij} = -\frac{1}{n} \int \rho (\eta_i - u_i) (\eta_j - u_j) \phi dV_\eta + p \delta_{ij} \quad 2.1.1e$$

$$s = k_B N - k_B V \int \phi \ln \left(\frac{h^3}{m^3} \phi \right) dV_\eta \quad 2.1.1f$$

In equation 2.1.1f, h is Planck's constant and N is the number of molecules within volume V . Further discussion on the definition of entropy can be found in [22]. It is common to refer to the various macroscopic properties as moments of the distribution function. The k^{th} moment, defined as Q^k , of the distribution function is given by:

$$Q^k = \frac{1}{n} \int |\eta_i - u_i|^k \phi dV_\eta \quad 2.1.2$$

The temperature is proportional to the 2nd moment of the distribution and the heat flux is proportional to the 3rd moment.

SCALING THE MOMENTS OF THE DISTRIBUTION FUNCTION:

It is often convenient to work with scaled variables. Velocities are scaled by a characteristic thermal speed, η_r , distances are scaled by a reference mean free path, and time is scaled by a reference collision time. The speed η_r has a physical meaning in that it is the most probable speed for a gas in equilibrium at a reference temperature.

$$\eta_r = \sqrt{\frac{2k_b T_r}{m}} \quad 2.1.3$$

The reference temperature and density are defined as T_r and n_r . The reference mean free path is computed via $\lambda_r = 1/(n_r \sigma_r)$ where σ_r is a reference collision cross section.

Scaled variables are denoted by a hat, and the scaled macroscopic variables become:

$$\hat{n} = \int_{\eta} \hat{\phi} dV_{\hat{\eta}} \quad 2.1.4a$$

$$\hat{u}_i = \frac{1}{\hat{n}} \int_{\eta} \hat{\eta}_i \hat{\phi} dV_{\hat{\eta}} \quad 2.1.4b$$

$$\hat{T} = \frac{2}{3\hat{n}} \int_{\eta} (\hat{\eta}_i - \hat{u}_i)^2 \hat{\phi} dV_{\hat{\eta}} \quad 2.1.4c$$

$$\hat{p} = \frac{1}{3} \int_{\eta} (\hat{\eta}_i - \hat{u}_i)^2 \hat{\phi} dV_{\hat{\eta}} = \frac{1}{2} \hat{n} \hat{T} \quad 2.1.4d$$

$$\hat{\tau}_{ij} = -2 \int_{\eta} (\hat{\eta}_i - \hat{u}_i) (\hat{\eta}_j - \hat{u}_j) \hat{\phi} dV_{\hat{\eta}} + \hat{p} \delta_{ij} \quad 2.1.4e$$

$$\hat{q}_j = \frac{1}{2} \int_{\eta} (\hat{\eta}_j - \hat{u}_j) (\hat{\eta}_i - \hat{u}_i)^2 \hat{\phi} dV_{\hat{\eta}} \quad 2.1.4f$$

It is less obvious how to scale the entropy. For this work, the entropy is scaled by the species gas constant R_s :

$$\hat{s} = B - \frac{1}{\hat{n}} \int_{\eta} \hat{\phi} \ln \hat{\phi} dV_{\eta}, \quad 2.1.4g$$

where B is an additive constant that cancels out when entropy differences are computed.

When applied to a discrete set of points in velocity space, the distribution function is viewed as a set of delta functions located at each grid point. Instead of having a continuum of velocities, the velocity space is quantized by the grid spacing β_v , defined with respect to non-dimensional variables. A Riemann sum integration routine is used to obtain the macroscopic properties and moments of the distribution. All of the mass in a volume surrounding a given velocity grid point is represented by a delta function located at that grid point, figure 2.1.1. This formulation differs from a histogram view of the distribution function. In a histogram view of the distribution, instead of the mass around a grid point being concentrated at a single point, it is distributed over a finite width bar.

Since the bar has a finite width, a single bar has a non-zero temperature whereas a single delta function has no corresponding temperature.

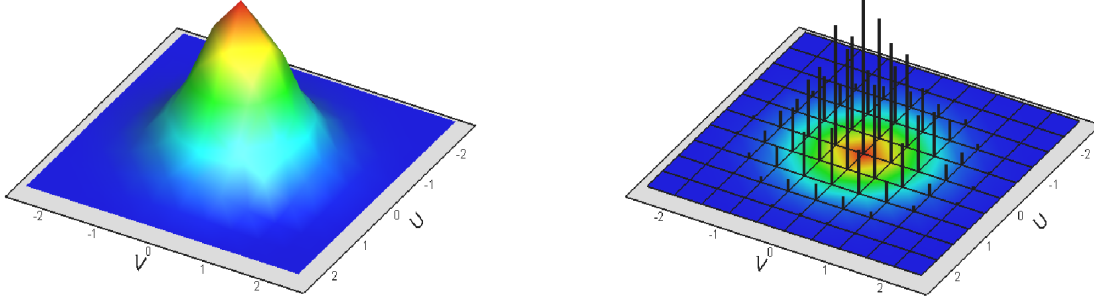


Figure 2.1.1. On the left side, a planar slice of a continuous velocity distribution is plotted. The right hand side is the delta function approximation to the continuous velocity distribution function.

Section 2: The Boltzmann Equation

The Boltzmann equation describes the time evolution of the velocity distribution function

$$\frac{\partial \phi}{\partial t} + \eta_i \frac{\partial \phi}{\partial x_i} = n^2 \int_{\eta} \int_{\Omega} [\phi(\eta'_i) \phi(\zeta'_i) - \phi(\eta_i) \phi(\zeta_i)] g \frac{\partial \sigma}{\partial \Omega} d\Omega dV_{\eta}. \quad 2.2.1$$

The effects of body forces have been neglected in the equation above. When scaled, the Boltzmann equation can be rewritten as:

$$\frac{\partial \hat{\phi}}{\partial \hat{t}} + \hat{\eta}_i \frac{\partial \hat{\phi}}{\partial \hat{x}_i} = \frac{1}{Kn} \int_{\hat{\eta}} \int_{\hat{\Omega}} [\hat{\phi}(\hat{\eta}'_i) \hat{\phi}(\hat{\zeta}'_i) - \hat{\phi}(\hat{\eta}_i) \hat{\phi}(\hat{\zeta}_i)] \hat{g} \frac{\partial \hat{\sigma}}{\partial \hat{\Omega}} d\hat{\Omega} dV_{\hat{\eta}} \quad 2.2.2$$

The Knudsen number, Kn , is the ratio between the mean free path and a characteristic length scale of the problem and is used to quantify the rarefaction of a flow. The left hand side of this equation represents the time rate of change of the number of molecules in a given point in velocity space by convection through the surfaces of the spatial element. The right hand side of the equation represents the changes in velocity space as a

result of collisions. The primed values indicate post-collision velocities and $\partial\sigma/\partial\Omega$ is the differential cross section. The collision integral is nonlinear and can be decomposed into depleting and replenishing collisions. It is convenient to separate the collision integral into depleting collisions and replenishing collisions because the proposed method pairs depleting collisions with their corresponding replenishing collisions to ensure conservation of mass, momentum, and energy.

$$\hat{I}_{coll} = \hat{I}_{repl} - \hat{I}_{depl} \quad 2.2.3a$$

$$\hat{I}_{depl} = \int_{\hat{\zeta}} \int_{\hat{\Omega}} \left[\hat{\phi}(\hat{\zeta}_i) \hat{\phi}(\hat{\eta}_i) \right] \hat{g} \frac{\partial \hat{\sigma}}{\partial \hat{\Omega}} d\hat{\Omega} dV_{\hat{\zeta}} \quad 2.2.3b$$

$$\hat{I}_{repl} = \int_{\hat{\zeta}} \int_{\hat{\Omega}} \left[\hat{\phi}(\hat{\zeta}_i') \hat{\phi}(\hat{\eta}_i') \right] \hat{g} \frac{\partial \hat{\sigma}}{\partial \hat{\Omega}} d\hat{\Omega} dV_{\hat{\zeta}} \quad 2.2.3c$$

Depleting collisions reduce the number of molecules within a certain velocity class and replenishing collisions add molecules to that velocity class. The post-collision velocities $\hat{\zeta}_i'$ and $\hat{\eta}_i'$ that appear in the replenishing integral are not independent variables but are determined from $\hat{\zeta}_i$ and $\hat{\eta}_i$ from the dynamics of an elastic collision.

The differential cross section describes the collision scattering and intermolecular potential between molecules. For many engineering applications the differential cross section is assumed to be isotropic, so integration over all scattering angles yields the total cross section, σ_T . There are numerous models that are used to describe the total cross section, such as Lennard-Jones [23], hard sphere models, variable hard spheres (VHS)[24], and variable soft spheres (VSS) [25]. In the present numerical scheme, a VHS model is used. The cross section in a VHS model, written in scaled variables, is given by $\hat{\sigma}_T = \hat{g}^{-\kappa}$ where κ is typically fractional. The cross section is scaled by a reference cross section and the relative speed is scaled by η_r . When $\kappa=0$ the collision cross section reduces to a hard sphere model. When $\kappa=1$ the total cross section

corresponds to pseudo-Maxwell molecules. Pseudo-Maxwell molecules are not identical to “real” Maxwell molecules because the scattering for “real” Maxwell molecules is not isotropic whereas in the VHS model the scattering is isotropic. If pseudo-Maxwell molecules are used, the Boltzmann equation for a homogeneous isotropic gas, simplifies to:

$$\frac{\partial \hat{\phi}}{\partial \hat{t}} \Delta \hat{t} = \frac{1}{Kn} [\Delta \hat{\phi}_{repl} - \Delta \hat{\phi}_{depl}] \quad 2.2.4a$$

$$\Delta \hat{\phi}_{depl} = \Delta \hat{t} \int_{\hat{\zeta}_i} \hat{\phi}(\hat{\zeta}_i) \hat{\phi}(\hat{\eta}_i) \hat{g} \hat{\sigma}_T d\hat{\zeta}_i = \Delta \hat{t} \hat{\phi}(\hat{\eta}_i) \int_{\hat{\zeta}_i} \hat{\phi}(\hat{\zeta}_i) d\hat{\zeta}_i \quad 2.2.4b$$

$$\Delta \hat{\phi}_{repl} = \Delta \hat{t} \int_{\hat{\zeta}_i} \hat{\phi}(\hat{\zeta}_i') \hat{\phi}(\hat{\eta}_i') d\hat{\zeta}_i \quad 2.2.4c$$

Equation 2.2.4b can be used to calculate the incremental depletion at grid point $\hat{\eta}_i$ as a result of depleting collisions. Equation 2.2.4c represents the incremental gain at grid point $\hat{\eta}_i$ as a result of replenishing collisions. The incremental depletion is a function of the pre-collision velocities $\hat{\eta}_i$ and $\hat{\zeta}_i$ and can therefore be evaluated directly. The incremental replenishment is not as easily computed because the post collision velocities depend upon the nature of the collision. For elastic collisions mass, momentum, and translational energy are conserved. For momentum to be conserved during a collision, the center of mass velocity remains constant. To satisfy energy conservation and momentum conservation, the magnitude of the relative velocity vector must also remain constant. For isotropic scattering, the direction of the post-collision relative velocity vector is distributed uniformly on the unit sphere centered about the center of mass velocity.

Section 3: 1D Shock Wave Theory

In this section, I discuss the theory behind traveling shock waves. A normal shock wave transitions a supersonic gas upstream of the wave to a subsonic flow

downstream of the shock wave. In continuum dynamics a shock is generally regarded as an abrupt change in macroscopic properties and the ratios between the upstream and downstream properties are described by the Rankine-Hugoniot conditions. In scaled variables, the Rankine-Hugoniot equations are:

$$\frac{\hat{\rho}_2}{\hat{\rho}_1} = \frac{(\gamma+1)M_1^2}{(\gamma-1)M_1^2 + 2} \quad 2.3.1a$$

$$\frac{\hat{T}_2}{\hat{T}_1} = \left[2 + (\gamma-1)M_1^2 \right] \frac{2\gamma M_1^2 - (\gamma-1)}{(\gamma+1)^2 M_1^2} \quad 2.3.1b$$

$$\frac{\hat{p}_2}{\hat{p}_1} = \frac{1}{(\gamma+1)} \left[2\gamma M_1^2 - (\gamma-1) \right] \quad 2.3.1c$$

For the traveling shock analyzed in Chapter 4.3, $\hat{u}_1 < 0$ and the gas downstream of the shock is at rest with respect to the lab reference frame. The shock speed, \hat{u}_s , with respect to the lab reference frame can be computed from continuum dynamics by solving the following quadratic equation:

$$\hat{u}_s^2 - \frac{3-\gamma}{2} \hat{u}_1 \hat{u}_s - \frac{1}{2} \left[\gamma + (\gamma-1) \hat{u}_1^2 \right] = 0, \quad 2.3.2$$

where \hat{u}_1 is the velocity of the unshocked gas. The upstream flow velocity relative to the shock is $(\hat{u}_s - \hat{u}_1)$ and the corresponding shock Mach number is $(\hat{u}_s - \hat{u}_1) \sqrt{2/\gamma}$.

In reality shocks have a finite thickness and the macroscopic properties inside of the shock wave depend on the nature of the molecular interactions. The thickness of a shock wave is commonly defined as the distance required to span the density change by the maximum density gradient. The thickness of the shock wave depends on how quickly the gas equilibrates. Shock waves generated with a hard sphere molecular model are thinner than shock waves composed of pseudo-Maxwell molecules. Commonly the shock thickness is expressed as a multiple of the upstream mean free path. The most general definition of the mean free path is given by:

$$\lambda = \frac{\langle c' \rangle}{n \langle \sigma g \rangle} \quad 2.3.4$$

The bracketed quantities are averaged and c' is the mean thermal speed of the gas. For hard sphere molecules the upstream mean free path is easily defined as:

$$\lambda_{upstream} = \frac{1}{\sqrt{2}n\sigma} \quad 2.3.5$$

In [26, 27] Bird defines the mean free path for a variable hard sphere gas by:

$$\lambda_{upstream} = \frac{\left(\frac{T}{T_{ref}} \right)^\omega}{(2-\omega)^\omega \Gamma(2-\omega) \sqrt{2}n\sigma_{ref}} \quad 2.3.6$$

The parameter ω describes the variation of the collision cross section to the relative translational energy

$$\sigma = \sigma_{ref} \left(\frac{g^2}{c_{ref}^2} \right)^{-\omega}, \quad 2.3.7$$

and Bird defines a reference thermal speed via

$$c_{ref}^2 = 2(2-\omega)k_b T_r / m^*. \quad 2.3.8$$

Here m^* is the reduced mass in a binary collision, ($m^* = m/2$ for a single species gas), and c_{ref} is the mean relative speed of colliding VHS molecules in an equilibrium gas at T_r (not the relative speed of molecules chosen at random). For hard sphere molecules, ω is 0 and for pseudo-Maxwell molecules ω is 0.5.

CHAPTER 3: METHOD

The method of solving the Boltzmann equation for a discrete velocity gas is described in this chapter.

Section 1: Creating the Physical and Velocity Domains

First, the physical space is divided into cells and corresponding velocity distributions are initialized for each physical cell. The cell size for rarefied flows should be of the same order as the mean free path. Although any non-equilibrium distribution can be initialized, typically an equilibrium distribution with a prescribed density, temperature, and velocity is used. To initialize the velocity distribution function, a continuous Maxwellian computed from a given temperature and density is evaluated at the set of discrete points in velocity space. The Maxwellian distribution for a 3-D gas is:

$$\varphi^{eq}(\eta_i : n, u_i, T) = n \left(\frac{m}{2\pi k_b T} \right)^{3/2} \exp \left[-\frac{m}{2k_b T} (\eta_i - u_i)^2 \right] \quad 3.1.1$$

When scaled by the reference velocity, eq2.1.3, upstream number density and the temperature, the scaled equilibrium distribution becomes:

$$\hat{\varphi}^{eq}(\hat{\eta}_i : \hat{n}, \hat{u}_i, \hat{T}) = \hat{n} \left(\frac{1}{\pi \hat{T}} \right)^{3/2} \exp \left[-\frac{1}{\hat{T}} (\hat{\eta}_i - \hat{u}_i)^2 \right] \quad 3.1.2$$

The equilibrium distribution is defined as the distribution where all moments of the distribution are invariant under collisions. When the continuous distribution is projected onto the discrete set of points, the resulting discrete distribution is not necessarily in equilibrium. The slight non-equilibrium can contaminate a solution. Consequently, before the distribution function is allowed to convect it is first relaxed to local equilibrium by collisions.

Since the collision integral is computationally expensive, a rather coarse discrete representation must be used. When creating a velocity grid, both the range and the resolution of the grid are important. A normally infinite velocity space is truncated where the contribution to the first several moments of the distribution function become vanishingly small. The third moment, the heat flux, is the highest physical moment and the velocity distribution is truncated where the contributions to this moment goes to zero. The resolution of the grid can affect several different routines. The numerical error resulting from integration increases as the grid is coarsened. Although a continuous Maxwellian has a specified temperature, velocity and density, the computed density, velocity, and temperature from the corresponding discrete distribution will have errors associated with the numerical integration. Having a coarse resolution also restricts the potential velocities that the gas can have. Since a real gas has a continuum of velocities, a limited set of discrete velocities can restrict the accuracy of the computations. Typical values used for the scaled velocity spacing, $\hat{\beta}$, range from 0.5 to 0.7 and the velocity domain typically ranges over $\pm 2.5\eta_r \hat{T}^{1/2}$. The velocity domain needs to be expanded as the gas temperature and velocity increase.

NUMERICAL INTEGRATION:

In this scheme, the discrete distribution is represented by a set of delta functions, figure 3.1.1, located at each grid point. All of the mass around a grid point in velocity space is concentrated at that grid point. In this representation, the macroscopic properties are:

$$\hat{n} = \sum_{IJK} \hat{\phi}_{IJK} \hat{\beta}_V^3 \quad 3.1.3a$$

$$\hat{u}_i = \frac{1}{\hat{n}} \sum_{IJK} \hat{\eta}_{iIJK} \hat{\phi}_{IJK} \hat{\beta}_V^3 \quad 3.1.3b$$

$$\hat{T} = \frac{2}{3\hat{n}} \sum_{IJK} (\hat{\eta}_{i_{IJK}} - \hat{u}_i)^2 \hat{\phi}_{IJK} \hat{\beta}_V^3 \quad 3.1.3c$$

$$\hat{p} = \frac{1}{2} \hat{n} \hat{T} \quad 3.1.3d$$

$$\hat{\tau}_{ij} = -2 \sum_{IJK} (\hat{\eta}_{i_{IJK}} - \hat{u}_i) (\hat{\eta}_{j_{IJK}} - \hat{u}_j) \hat{\phi}_{IJK} \hat{\beta}_V^3 + \hat{p} \delta_{ij} \quad 3.1.3e$$

$$\hat{q}_j = \frac{1}{2} \sum_{IJK} (\hat{\eta}_j - \hat{u}_j) (\hat{\eta}_{i_{IJK}} - \hat{u}_{i_{IJK}})^2 \hat{\phi}_{IJK} \hat{\beta}_V^3 \quad 3.1.3f$$

$$\hat{s} = -\frac{1}{\hat{n}} \sum_{IJK} \hat{\phi}_{IJK} \ln(\hat{\phi}_{IJK}) \hat{\beta}_V^3 \quad 3.1.3g$$

The scaled velocity spacing parameter is β_V and I, J , and K are integer indices that denote position on the velocity grid.

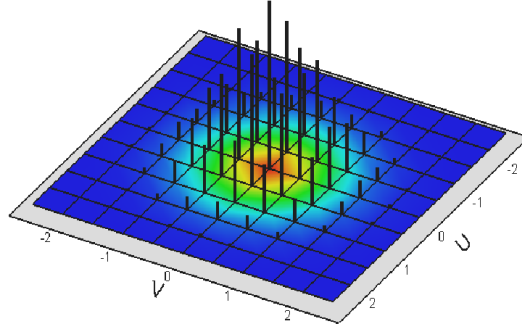


Figure 3.1.1. A discrete velocity distribution function represented by a set of delta functions.

Once a suitable discrete representation of the velocity distribution function is created, the Boltzmann equation can be solved by performing collision steps followed by convective steps.

TIME SPLITTING METHOD

To solve the Boltzmann equation, the collision integral and the convective terms are solved separately.

$$\Delta \hat{\phi} \equiv \frac{\partial \hat{\phi}}{\partial \hat{t}} \Delta \hat{t} = \Delta \hat{\phi}_{collision} + \Delta \hat{\phi}_{convection} \quad 3.1.4$$

$$\Delta \hat{\phi}_{convection} = -\hat{\eta}_i \frac{\partial \hat{\phi}}{\partial \hat{x}_i} \Delta \hat{t} \quad 3.1.5$$

$$\Delta \hat{\phi}_{collision} = \hat{I}_{coll} \Delta \hat{t} \quad 3.1.6$$

Section 2: Collisions

The collision integral can be decomposed into depleting and replenishing collisions. Replenishing collisions add molecules to a certain velocity class and depleting collisions remove mass from a certain velocity class. The depleting collision rate at velocity point $\hat{\eta}_i$ is obtained by integrating equation 3.2.1b over all possible scattering angles and all collision partner velocities. The replenishing collision rate at $\hat{\eta}_i$ can be obtained by integrating equation 3.2.1c over all collisions that produce velocities $\hat{\eta}_i$.

$$\hat{I}_{coll} = \hat{I}_{repl} - \hat{I}_{depl} , \quad 3.2.1a$$

$$\hat{I}_{depl} = \int \int_{\hat{\xi} \hat{\Omega}} [\hat{\phi}_{\hat{\xi}} \hat{\phi}_{\hat{\eta}}] \hat{g} \frac{\partial \hat{\sigma}}{\partial \hat{\Omega}} d\hat{\Omega} dV_{\hat{\xi}} , \quad 3.2.1b$$

$$\hat{I}_{repl} = \int \int_{\hat{\xi} \hat{\Omega}} [\hat{\phi}_{\hat{\xi}} \hat{\phi}_{\hat{\eta}_i}] \hat{g} \frac{\partial \hat{\sigma}}{\partial \hat{\Omega}} d\hat{\Omega} dV_{\hat{\xi}} . \quad 3.2.1c$$

One way to solve the collision integral such that mass, momentum, and energy are conserved is to pair replenishing collisions with their corresponding direct depleting collisions.

DEPLETING COLLISIONS

For isotropic scattering the angular dependence can be integrated immediately and the incremental depletion at a given point $\hat{\eta}_i$ is given by

$$\Delta\hat{\phi}_{depl} = \Delta\hat{t} \int_{\hat{\zeta}_i} \hat{\phi}(\hat{\zeta}_i) \hat{\phi}(\hat{\eta}_i) \hat{g} \hat{\sigma}_T d\hat{\zeta}_i. \quad 3.2.2$$

If pseudo-Maxwell molecules are used, $\hat{g} \hat{\sigma}_T = 1$, and equation 3.2.2 simplifies to

$$\Delta\hat{\phi}_{depl} = \Delta\hat{t} \hat{\phi}(\hat{\eta}_i) \hat{n} \quad 3.2.3$$

In previous work, the collision integral was evaluated by considering collisions between each point $\hat{\eta}_i$ and all other points $\hat{\zeta}_j$. This method is $O(N_V^2)$, where for each collision between point $\hat{\eta}_i$ and $\hat{\zeta}_j$ the corresponding incremental depletion is:

$$\Delta\hat{\phi}_{depl}(\hat{\zeta}_i) = \frac{1}{2} \Delta\hat{t} \hat{\phi}(\hat{\zeta}_i) \hat{\phi}(\hat{\eta}_i), \quad 3.2.4a$$

$$\Delta\hat{\phi}_{depl}(\hat{\eta}_i) = \frac{1}{2} \Delta\hat{t} \hat{\phi}(\hat{\zeta}_i) \hat{\phi}(\hat{\eta}_i). \quad 3.2.4b$$

By integrating over all possible collisions between $\hat{\eta}_i$ and $\hat{\zeta}_j$, the depleting integral is evaluated exactly within the discretization error. The factor of one half is to prevent double counting. Although this results in correct evaluation of the depleting integral, it is computationally expensive and of order N_V^2 , where N_V is the number of points in velocity space. Throughout the remainder of this report, this method of evaluating the collision integral will be referred to as the N^2 method. To reduce the computational effort associated with the N^2 method, the depleting integral is evaluated statistically by considering collisions between each point $\hat{\eta}_i$ and a set of randomly chosen collision partners, M_j , figure 3.2.1. To do this, the incremental depletion at $\hat{\eta}_i$ is analytically computed from equation 3.2.3. Next a set of random collision partners, M_j is chosen by a selection algorithm as described below.

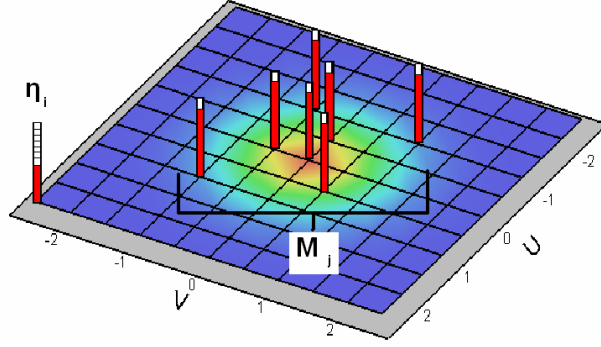


Figure 3.2.1. A set of random collision partners M_j is chosen to collide with η_i . The selection of collision partners biases those that contribute more to the collision integral.

PICKING COLLISION PARTNERS

Many points in velocity space contain trace amounts of mass, especially near the fringes of the domain and consequently they contribute little to the collision integral. The goal of the proposed selection algorithm is to efficiently select collision partners that contribute more to the collision integral. A simple way to do this is to use an acceptance rejection algorithm that biases collision partners that contribute more to the collision integral. For Maxwell molecules, the contribution to the depleting collision integral is directly proportional to the value of the distribution function. In traditional acceptance-rejection schemes two random numbers are drawn. First a random point in velocity space is selected. To select a point in velocity space one can generate three random numbers corresponding to the three directions of velocity, but it is computationally expensive to call three random numbers. Alternatively, it is possible to select a random point by calling one random number. A random number, l , is defined as an integer between 0 and N_v-1 . The index l can be mapped to indices I , J , and K by the following equations:

$$K = MOD(l, R_k) + k_{\min} \quad 3.2.5a$$

$$J = MOD\left(\text{int}\frac{l}{R_k}, R_j\right) + j_{\min} \quad 3.2.5b$$

$$I = \text{int}\left[\frac{\text{int}\frac{l}{R_k}}{R_j}\right] + i_{\min} \quad 3.2.5c$$

The ranges R_k and R_j are given by:

$$R_k = k_{\max} - k_{\min} + 1, \quad 3.2.5d$$

$$R_j = j_{\max} - j_{\min} + 1, \quad 3.2.5e$$

Where, e.g. k_{\min} and k_{\max} correspond to the minimum and maximum integer indices for the parameter K . These mapping equations allow for a single random number call to select a point in 3-D velocity space defined by (I, J, K) . A second random number is generated after the first random point is selected. If the local value of the distribution function is larger than the second random number, that point is accepted. If it is not accepted, a new set of random numbers is drawn. This scheme can be computationally intensive because of the costs associated with generating random numbers.

Alternatively, the process of selecting random collision partners can be made more efficient by creating a cumulative distribution function Ψ .

$$\Psi(s) = \sum_l^s |\hat{\phi}_{lJK}| \quad 3.2.6$$

The function $\Psi(s)$ increases monotonically from $s=0$ to $s=(N_v-1)$. A random number R between 0 and $\Psi(s)$ is drawn. A binary search is then used to find the value l such that R lies between $\Psi(l)$ and $\Psi(l+1)$. Since the increment between $\Psi(l+1)$ and $\Psi(l)$ is $|\phi_l|$, points in velocity space with more mass are more likely to be chosen than points with little mass, figure 3.2.2.

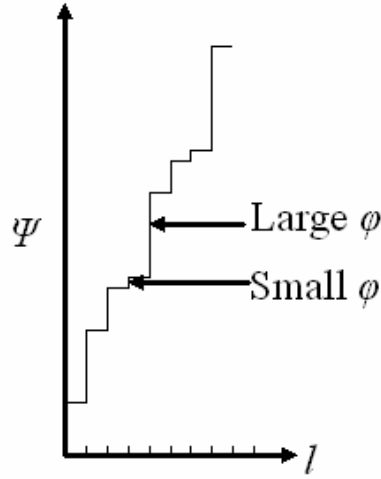


Figure 3.2.2. A sample plot of the cumulative distribution function Ψ . Large steps correspond to large values of ϕ and smaller steps correspond to smaller values of ϕ .

The cumulative scheme avoids having to reject randomly sampled points, based on another random number call, and thus reduces the number of random number calls in two ways. However, as noted above, a search is required. Collision partners can be selected more than once and partners are selected continuously until the set of random collision partners has a mass fraction larger than a cutoff mass fraction. The cutoff fraction is referred to as the depleting fraction, DF.

For a test velocity $\hat{\eta}_i$ colliding with a set of field velocities, M_j , the amount depleted, Eq. 3.2.7a, is evenly distributed among all collision pairs. For further information, refer to Appendix A.

$$d \equiv \frac{1}{2} \Delta \hat{t} \hat{\phi}(\hat{\eta}) (\hat{n} - 2\hat{n}_{neg} - |\hat{\phi}(\hat{\eta})| \beta^3) \text{sgn}(\phi(\hat{\xi})) \quad 3.2.7a$$

REPLENISHING COLLISIONS

The inverse replenishing collisions are computed along with the corresponding direct depleting collisions. For elastic collisions mass, momentum, and energy are

conserved and in a discrete velocity framework, all possible collision outcomes lie on the sphere of diameter g centered about the center of mass velocity, figure 3.2.3.

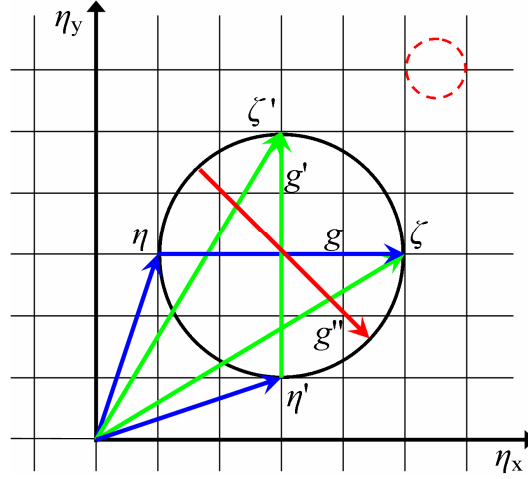


Figure 3.2.3. Collision circle drawn in 2D. Elastic collisions between η and ζ result in post collision velocities that lie on the black circle. The blue lines represent the pre-collision velocities and the green and red lines are post-collision velocities.

In the two-dimensional figure 3.2.3 the depleting collisions are performed at η and ζ corresponding to the blue vectors. To find the post collision velocities, the relative velocity vector g is arbitrarily rotated about the center of mass velocity. These replenishing velocities correspond to the red and green vectors. In principle the replenishing integral is evaluated by considering all possible post-collision velocities. The integral is approximated by sampling several replenishing pairs. The total amount replenished equals the amount depleted for each collision, ensuring mass, momentum, and energy conservation. The replenishment is then shared equally among all post-collision velocities. In a discrete representation, the only permissible velocities are those that lie precisely on the velocity grid. Figure 3.2.3 shows that this restriction can limit the number of post collision velocities. In general, as the relative velocity vector becomes smaller, the number of potential post-collision velocities that lie on the grid

decreases [28]. For collisions between molecules with very small relative velocities, there may be no post-collision velocities that lie on the grid. In figure 3.2.3, this null type of collision is represented by the red circle. The reduction of possible collision outcomes can artificially restrict the approach to equilibrium. Consequently, we present an approach wherein the post-collision velocities that lie off the grid (e.g. g'' in Fig. 3.2.3) are projected onto the discrete grid so that mass, momentum, and energy are conserved [12].

INTERPOLATION SCHEME

While projecting mass changes, $\Delta\phi$, that lie off the grid back onto the grid, the 5 conservation equations must be satisfied. First, a stencil in which the contribution $\Delta\phi$ is mapped to needs to be defined. The origin of the stencil, the green point in figure 3.5, is taken as the velocity lattice point closest to the mass increment to be interpolated. That mass increment is located at coordinates a, b , and c . The origin and three other points that lie on the cube surrounding the interpolating point make up the ‘interior points’. These points are denoted by the blue and green dots in figure 3.2.4.

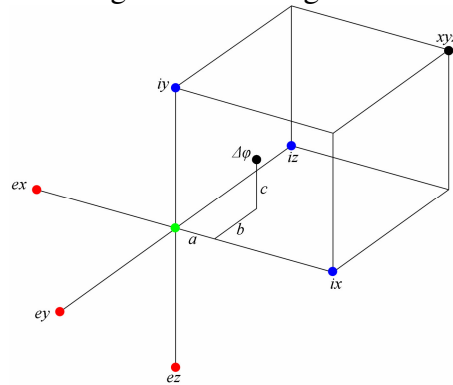


Figure 3.2.4. A 7-point symmetric stencil when the point to be interpolated lies within the cubic velocity domain.

Although it would appear logical to use a 5th point located on the cube surrounding the interpolating point, e.g. point xyz , the resulting matrix describing mass, momentum, and energy conservation is singular. However, it is possible to obtain a unique interpolation onto the grid by using 4 ‘internal’ points that lie on the cube surrounding the mass increment (three blue and one green) and a 5th ‘external’ point that is outside of the box. One ‘external’ point ex , ey , or ez would suffice, but to preserve symmetry, three external points are used and the interpolation is shared evenly to all three ‘external’ points. The conservation equations for such a symmetric 7-point stencil with three ‘external’ points are:

$$\begin{array}{l} \text{mass} \\ x-mom \\ y-mom \\ z-mom \\ \text{energy} \end{array} \begin{pmatrix} 1 & 1 & 1 & 1 & 3 \\ 0 & 1 & 0 & 0 & -1 \\ 0 & 0 & 1 & 0 & -1 \\ 0 & 0 & 0 & 1 & -1 \\ 0 & 1 & 1 & 1 & 3 \end{pmatrix} \begin{pmatrix} f_o \\ f_{ix} \\ f_{iy} \\ f_{iz} \\ f_{ext} \end{pmatrix} = \begin{pmatrix} 1 \\ a \\ b \\ c \\ a^2 + b^2 + c^2 \end{pmatrix} \quad 3.2.8$$

The parameters a , b , and c are the components of the relative velocity vector from the stencil origin at o to the point to be interpolated. The values f_o , f_{ix} , f_{iy} , f_{iz} , and f_{ext} are the fractional amounts of mass that are interpolated to each corresponding point. This matrix is invertible, and the corresponding interpolation equations for a symmetric 7-point stencil are:

$$\begin{aligned} f_o &= 1 - a^2 - b^2 - c^2 \geq 0 \\ f_{ext} &= -(a + b + c - a^2 - b^2 - c^2)/6 \leq 0 \\ f_{ix} &= (a + f_{ext}) \\ f_{iy} &= (b + f_{ext}) \\ f_{iz} &= (c + f_{ext}) \end{aligned} \quad 3.2.9$$

For the stencil shown above, the interpolation equations always result in negative changes at the external points of the stencil. The negative mass change is necessary to

satisfy the energy constraint because the only way to cancel the relative kinetic energy introduced by distributing the mass to different velocities is to introduce a decrease in mass somewhere.

The interpolation equations (eq 3.2.9) were derived for the common case where the point to be interpolated lies within the velocity space domain. Occasionally collisions yield velocities that are outside the domain, as is the case in figure 3.2.5.

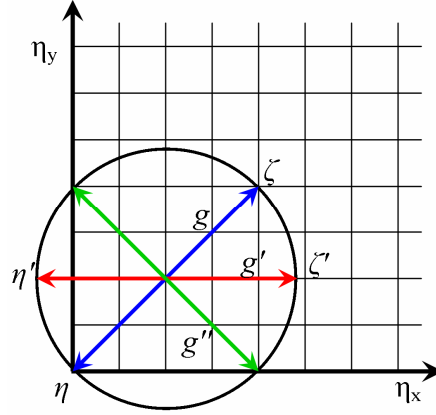


Figure 3.2.5. A collision that results in a post collision velocity that lies outside of the domain.

Using a similar procedure, it is also possible to map these points to the nearest stencil on the grid. To construct the stencil, the nearest point in velocity space that is not a corner of the cubic velocity domain is selected as the stencil origin. A corner of the velocity domain is not an acceptable stencil origin because it only has three points as neighbors and a 5 point stencil is required at a minimum. The internal points are then selected as the next three nearest points that form the cube that is closest to the point to be interpolated. Only one or two ‘exterior’ points are used if the stencil origin is on an edge of the velocity domain or a face boundary of the domain. For example, in figure 3.2.6, the origin corresponds to a point that is on the edge of the velocity domain and only one exterior point is used.

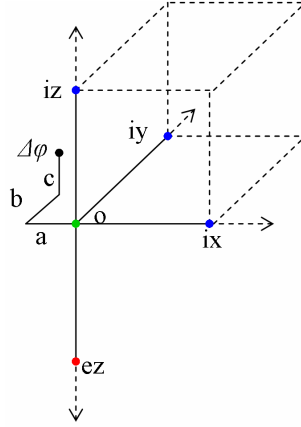


Figure 3.2.6. A 5-point stencil (o , ix , iy , iz , ez) where the point to be interpolated lies outside of the velocity domain and is mapped back into the defined velocity space. The line connecting points iz and ez represent an edge of the velocity domain.

The corresponding matrix describing mass, momentum, and energy conservation is:

$$\begin{matrix} \text{mass} \\ x\text{-mom} \\ y\text{-mom} \\ z\text{-mom} \\ \text{energy} \end{matrix} \begin{pmatrix} 1 & 1 & 1 & 1 & 1 \\ 0 & 1 & 0 & 0 & 0 \\ 0 & 0 & 1 & 0 & 0 \\ 0 & 0 & 0 & 1 & -1 \\ 0 & 1 & 1 & 1 & 1 \end{pmatrix} \begin{pmatrix} f_o \\ f_{ix} \\ f_{iy} \\ f_{iz} \\ f_{ez} \end{pmatrix} = \begin{pmatrix} 1 \\ a \\ b \\ c \\ a^2 + b^2 + c^2 \end{pmatrix} \quad 3.2.10$$

Similar to the previous stencil, a , b , and c are the components of the relative velocity vector from the stencil origin to the interpolating point. In figure 3.6, a is a negative number and b and c are positive numbers. For the stencil above, the interpolation equations are:

$$\begin{aligned} f_o &= 1 - a^2 - b^2 - c^2 \\ f_{ez} &= -(a + b + c - a^2 - b^2 - c^2)/2 \\ f_{ix} &= a \\ f_{iy} &= b \\ f_{iz} &= c + f_{ez} \end{aligned} \quad 3.2.11$$

When interpolating post-collision mass increments that extend off the grid back onto the grid, a penalty is paid by the creation of larger negative changes of mass. Since the point to be interpolated does not lie within the cube defined by the ‘interior’ points and origin, the negative changes of mass can occur at the external points or interior points. In particular, one can map any point to the above 5-point stencil and conserve mass, momentum, and energy regardless of the orientation of the interpolating point relative to the stencil origin. As the distance from the interpolating point to the stencil origin increases, however, more negative mass must be created to satisfy the conservation equations. Therefore, for the case where an interpolating point is far from an origin, i.e. for points well outside of the domain, appreciable negative changes in mass must be created. In general this is not a serious problem because collisions that result in velocities that lie outside of the grid boundaries are infrequent and the fractional masses that are moved back onto the grid are very small, of the order 10^{-6} .

After the replenishing velocities are mapped back onto the grid, collisions between η_i and the remainder of the random collision partner set M_j are considered. The process is then repeated for all η_i points in velocity space.

NEGATIVE MASS

Occasionally, portions of the distribution function can become negative if the interpolation or collision cause more mass to be depleted from a point than that point has available. In general, this negative mass is carried along with the solution even though negative mass is unphysical. Typically the magnitudes of the negative values are very small, $O(10^{-4})$. The only apparent problem with this is that the negative values make it difficult to evaluate the entropy because the entropy depends on $\ln(\varphi)$, *cf.* equation 3.1.3g, which is undefined for $\varphi < 0$. There are four different options to evaluate the entropy. The first method is to assume that the negative values are negligible and not include their

contributions to the overall entropy. It is easily shown that $\lim_{\phi \rightarrow 0} (\phi \ln \phi) = 0$. This method generally results in over-predicting the entropy. Another way is to modify the definition of entropy such that:

$$\hat{s} = -\frac{1}{\hat{n}} \sum_{IJK} \hat{\phi}_{IJK} \ln |(\hat{\phi}_{IJK})| \hat{\beta}_V^3 \quad 3.2.12$$

When all points in velocity space are positive, this definition of entropy is equivalent to equation 3.1.3g and the entropy is predicted correctly. A third way to evaluate the entropy is to remove the negative mass by a “sweeping” algorithm. Removing the negative values of the distribution is only performed to compute the entropy, and does not actually change the distribution function. Sweeping is done by first calculating the pre-sweep momentum components, density, and temperature of the distribution. All of the negative values of $\hat{\phi}$ are then set to zero and the distribution function is then rescaled to correct the mass back to its unswept state. The swept distribution function will have a slight error in the temperature and momentum, so additional corrections are imposed to conserve momentum and energy. These corrections are applied to a 27 point stencil centered about the origin in velocity space. The origin is the zero velocity point in velocity space. Momentum in the $\hat{\eta}_1$ direction is conserved by:

$$\begin{aligned} \hat{\phi}_{corr}(1,0,0) &= \hat{\phi}(1,0,0) - \frac{1}{2} \hat{u}_1^{err} \frac{\hat{n}}{\hat{\beta}_V^3} \\ \hat{\phi}_{corr}(-1,0,0) &= \hat{\phi}(-1,0,0) + \frac{1}{2} \hat{u}_1^{err} \frac{\hat{n}}{\hat{\beta}_V^3} \end{aligned} \quad 3.2.13a$$

where,

$$\hat{u}_1^{err} = \hat{u}_{swept} - \hat{u}_{pre-swept} \quad 3.2.13b$$

and similarly for the other two directions. To correct the energy, the error is first computed as:

$$\hat{T}_{err} = \frac{3}{2} \left(\hat{T}_{swept} - \hat{T}_{pre-swept} \right) \frac{\hat{n}}{\beta_V^3} \quad 3.2.14$$

At the origin, a small amount of mass is added:

$$\Delta \hat{\phi}_{origin} = \frac{13}{27 \beta^2} \hat{T}_{err} \quad 3.2.15a$$

At the other 26 points that surround the origin, a corresponding small amount of mass is subtracted.

$$\Delta \hat{\phi}_{ij} = -\frac{1}{26} \Delta \hat{\phi}_{origin} \quad 3.2.15b$$

Each of the previous three schemes are rather ad-hoc, where instead of evaluating the entropy of the distribution directly we perturb the distribution to remove the negative mass. Since in general only the change in entropy is important, the entropy can be alternatively computed by the Gibbs equation:

$$\Delta \hat{s} = \frac{s_2 - s_1}{R} = \frac{\gamma}{\gamma - 1} \ln \left(\frac{\hat{T}_2}{\hat{T}_1} \right) - \ln \left(\frac{\hat{P}_2}{\hat{P}_1} \right) \quad 3.2.16$$

Using Gibb's equation does not work for non-equilibrium distributions, so it is not helpful in general. However, the above equation can be used to obtain the correct jump conditions across a shock wave.

Section 3: Convection

In the time-splitting approach the change in the distribution function due to convection is computed after the collision step. The boundary conditions are applied during the convective step. The physical space is divided into a set of square cells and the velocity distribution function in each physical cell defines the local motion of the molecules. In this work a first order time explicit upwind scheme is used for the

convective step. Using an explicit expansion of the time derivative, the collision-less Boltzmann equation becomes:

$$\frac{\hat{\phi}(\hat{x}, \hat{t} + \Delta\hat{t}, \hat{\eta}_i) - \hat{\phi}(\hat{x}, \hat{t}, \hat{\eta}_i)}{\Delta\hat{t}} + \hat{\eta}_i \frac{\partial \hat{\phi}(\hat{x}, \hat{t}, \hat{\eta}_i)}{\partial \hat{x}_i} = 0 \quad 3.3.1$$

An upwind scheme that depends on the direction of the velocity is used for the spatial derivative:

$$\frac{\partial \hat{\phi}(\hat{x}_i, \hat{t}, \hat{\eta}_i)}{\partial \hat{x}_i} = \begin{cases} \frac{\hat{\phi}(\hat{x}_i + \Delta\hat{x}_i, \hat{t}, \hat{\eta}_i) - \hat{\phi}(\hat{x}_i, \hat{t}, \hat{\eta}_i)}{\Delta\hat{x}_i}, & \hat{\eta}_i < 0 \\ \frac{\hat{\phi}(\hat{x}_i, \hat{t}, \hat{\eta}_i) - \hat{\phi}(\hat{x}_i - \Delta\hat{x}_i, \hat{t}, \hat{\eta}_i)}{\Delta\hat{x}_i}, & \hat{\eta}_i > 0 \end{cases} \quad 3.3.2$$

When substituted into equation 3.3.1, the updated distribution function is:

$$\varphi(\hat{x}_i, \hat{t} + \Delta\hat{t}, \hat{\eta}_i) = \varphi(\hat{x}_i, \hat{t}, \hat{\eta}_i) - \Delta\hat{t} \hat{\eta}_i \begin{cases} \frac{\hat{\phi}(\hat{x}_i + \Delta\hat{x}_i, \hat{t}, \hat{\eta}_i) - \hat{\phi}(\hat{x}_i, \hat{t}, \hat{\eta}_i)}{\Delta\hat{x}_i}, & \hat{\eta}_i < 0 \\ \frac{\hat{\phi}(\hat{x}_i, \hat{t}, \hat{\eta}_i) - \hat{\phi}(\hat{x}_i - \Delta\hat{x}_i, \hat{t}, \hat{\eta}_i)}{\Delta\hat{x}_i}, & \hat{\eta}_i > 0 \end{cases} \quad 3.3.3$$

In order to be stable, the following CFL condition must be satisfied.

$$|\hat{\eta}_i|_{\max} \frac{\Delta\hat{t}}{\Delta\hat{x}} < 1 \quad 3.3.4$$

For the non-equilibrium flow problems of interest, the physical space step should be less than the mean free path. For a Mach 1.97 shock in an example in the next chapter, the velocity space is truncated at $|\hat{\eta}|_{\max} = 3.5$. Under these conditions, the time step for the convective term must be relatively small, less than 0.1. For higher Mach number flows, the maximum velocity increases and consequently the time step must be even smaller. Although not implemented in this work, it may be beneficial to use fractional substeps for the convective and collision routines. The convective step can be computed very quickly relative to the collision step, but the time step is limited only in the convective routine

and not in the collision routine. It may be beneficial to use a larger time step for collisions and a smaller time step for convection.

BOUNDARY CONDITIONS

For the 1D unsteady shock problem an equilibrium distribution moving to the left at a prescribed mean velocity is initialized for all physical cells. A specular boundary is imposed on the distribution function, ϕ^L , at the left boundary and the right boundary, ϕ^R , is set to have a zero gradient. To impose the specular boundary condition, the part of the distribution that convects to the left is mirrored to the right side.

$$\hat{\phi}^L(\hat{\eta}_1, \hat{\eta}_2, \hat{\eta}_3) = \hat{\phi}^L(-\hat{\eta}_1, \hat{\eta}_2, \hat{\eta}_3), \quad \hat{\eta}_1 > 0 \quad 3.3.5$$

By doing this, the molecules that are moving into the wall strike the wall and the normal component of velocity changes sign. The specular wall boundary condition also satisfies energy conservation. To impose the zero gradient boundary condition on the right side of the physical domain, the distribution function in the right-most cell is copied from the adjacent cell to the left.

CHAPTER 4: NUMERICAL RESULTS

Section 1: Spatially Homogeneous Relaxation

The major challenge to solving the Boltzmann equation involves evaluation of the non-linear collision integral. To isolate the collision scheme, homogeneous relaxation test cases were first implemented. The two distribution functions analyzed are the Bobylev-Krook-Wu (BKW) distribution and the Maxwellian distribution. Since the collision scheme is conservative, mass, momentum, and temperature should not change as the distribution relaxes. The BKW distribution starts as a non-equilibrium distribution that relaxes to a Maxwellian. There are two sources of error: (1) the discretization error – how many points in velocity space are used to approximate the distribution function, and (2) statistical or other errors from evaluating the collision integral stochastically. The errors associated with both sources are analyzed. A low depleting fraction and a coarse grid are desirable for efficient computation.

Varying Depleting Fraction and Replenishing Pairs

In this scheme it is possible to vary how accurately the depleting and replenishing integrals are evaluated by adjusting the depleting fraction and number of replenishing pairs. The depleting fraction is the mass fraction of the set of randomly chosen collision partners. The number of replenishing pairs represents how many post-collision velocity pairs are sampled, e.g. how many rotations of the relative velocity vector are performed. An 11^3 grid with a scaled velocity spacing of 0.5 and time step of 0.2 are used in the following test cases.

The relaxation of the Bobylev-Krook-Wu distribution using different depleting fractions is studied and these results are compared to the N^2 method. The N^2 method is a

computationally expensive scheme that considers all possible collision partners. In previous work, [12], it was found that 2 replenishing pairs are sufficient for a smooth solution, but 10 pairs are used to ensure that this solution approximates the exact solution very well. This solution ($O(N^2)$ with 10 replenishing pairs) is referred to as the “Gold Standard” (GS) for BKW relaxation. Analytic results can be obtained by projecting a continuous distribution function onto a discrete grid, but these results are not used because a continuous distribution function relaxes slightly differently than a discrete distribution function, with the discrete relaxation tending to the analytic result as the discretization becomes very fine.

Although the GS solution uses 10 replenishing pairs, the other simulations use 4 replenishing pairs. Figure 4.1.1 shows slices of the distribution function plotted at different times for a depleting fraction of 80%. A cubic spline is passed through the discrete data to guide the eye.

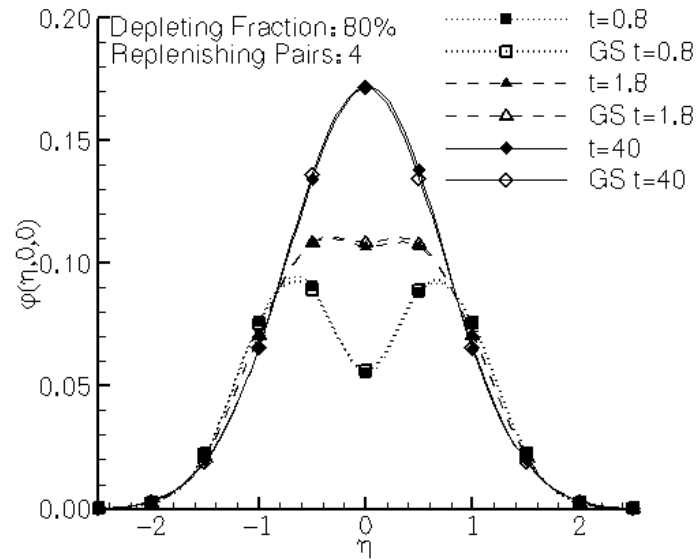


Figure 4.1.1 Instantaneous realizations of the Bobylev-Krook Wu distribution with a depleting fraction of 80% at three different times. For comparison are the corresponding GS solutions.

With this depleting fraction, an average of 175 collision partners are sampled per point in velocity space. This shows that with such a large depleting fraction, the numerical solution approximates the GS solution very closely.

Figure 4.1.2 shows that slices of the distribution still closely agree with the GS solution when the depleting fraction is reduced to 40%. An average of 70 collision partners are sampled per point in velocity space with this depleting fraction.

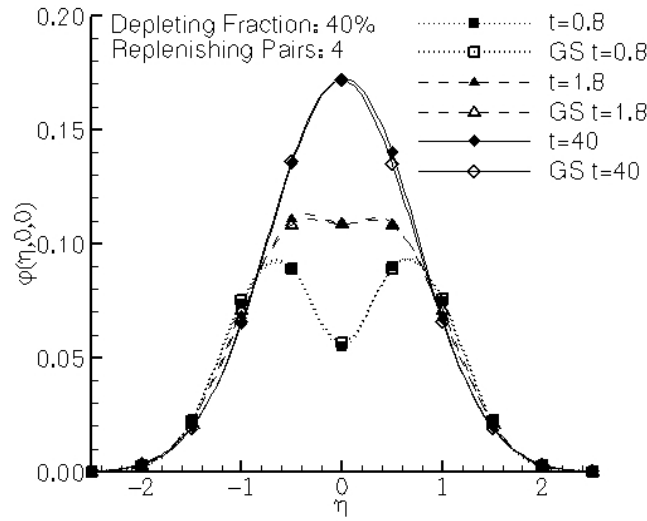


Figure 4.1.2. Instantaneous realizations of the BKW distribution with a depleting fraction of 40% at three different times.

When the depleting fraction is further decreased to 5% the noise increases significantly as shown in figure 4.1.3. This occurs because at lower depleting fractions larger amounts of mass are distributed among fewer points. An average of 7 collision partners are sampled per point in velocity space. Despite the increased noise for the 5% case, the computational time associated with this method is nearly two orders of magnitude smaller than the N^2 method. To reduce the noise, the 5% run was ensemble averaged and the resulting smooth distributions are compared to the GS results. By

ensemble averaging solutions generated with a 5% depleting fraction, the N^2 results can nearly be recovered.

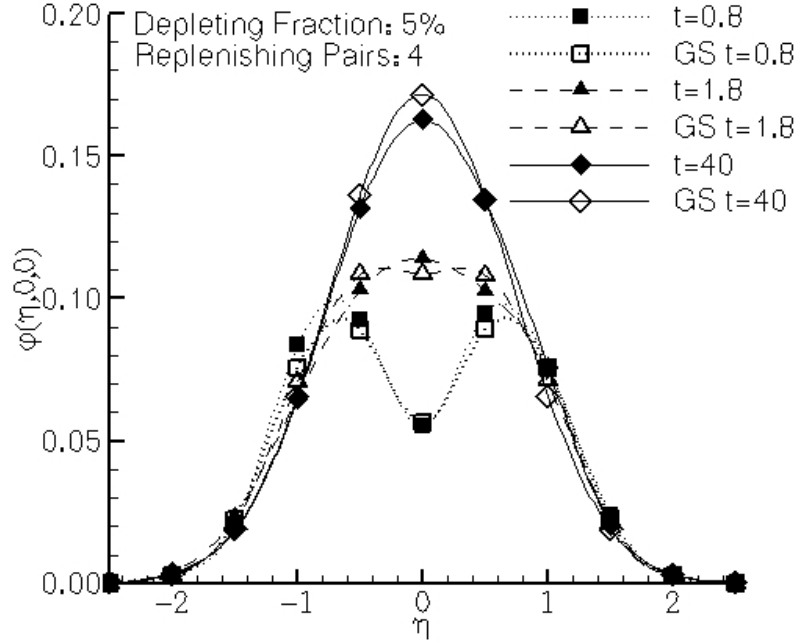


Figure 4.1.3. Un-averaged instantaneous realizations of the BKW distribution with a depleting fraction of 5% at three different times.

The macroscopic variables of interest are obtained by integrating different moments of the distribution function. The integration tends to smooth the macroscopic variables so even though the distribution function might be noisy, the variables of interest may be smooth. To assess the noise, the RMS difference between the computed distribution and the GS solution are plotted in 4.1.4. The RMS is defined as:

$$RMS = \sqrt{\sum_{IJK} (\varphi_{IJK}^{GS} - \varphi_{IJK}^{Computed})^2} \quad 4.1.1$$

As the distribution function is progressively ensemble averaged, the RMS decreases and the distribution converges towards the GS. It is difficult to draw a conclusion about the noise during the transient relaxation because the solution starts with smooth distribution

and the statistical fluctuations take several steps to grow. For transient problems ensemble averaging can become expensive, but for steady problems one can obtain acceptable results using very small depleting fractions.

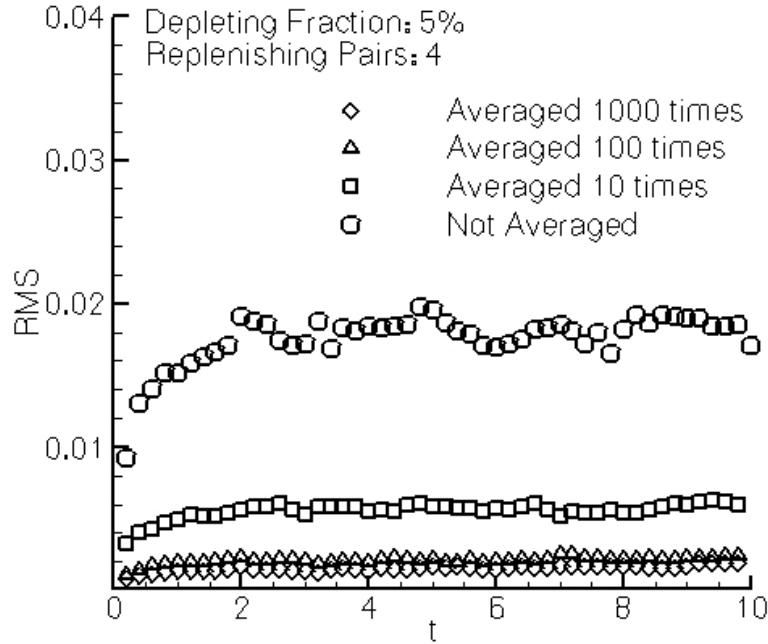


Figure 4.1.4. The RMS difference between an un-averaged GS solution and ensemble averaged solutions generated with a 5% depleting fraction.

In addition to the RMS, the computed entropy is very sensitive to the statistical noise. After ensemble averaging the 5% scheme over as few as 10 independent relaxations, the entropy converges to within 2% of the GS, figure 4.1.5. Statistical fluctuations cause the entropy to undershoot because the Maxwellian is defined as the maximum entropy distribution that is invariant under collisions, and any deviation away from that distribution due to statistical fluctuations will result in reduced entropy.

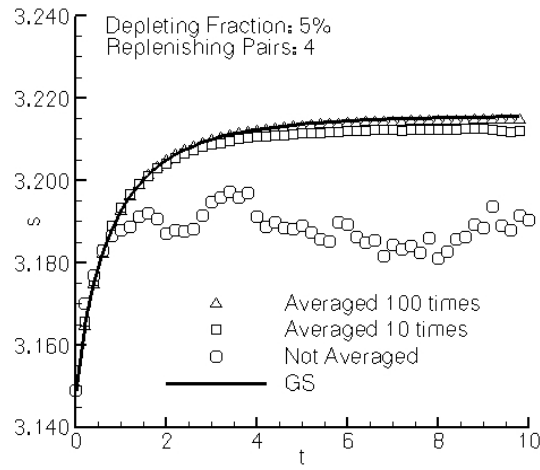


Figure 4.1.5. The entropy evolution for ensemble averaged solutions generated with a 5% depleting fraction compared to the N^2 solution.

In Figure 4.1.6, the entropy variation is plotted for depleting fractions of 80% and 40% to show that accurate transient solutions can be obtained without ensemble averaging provided an adequate depleting fraction is used.

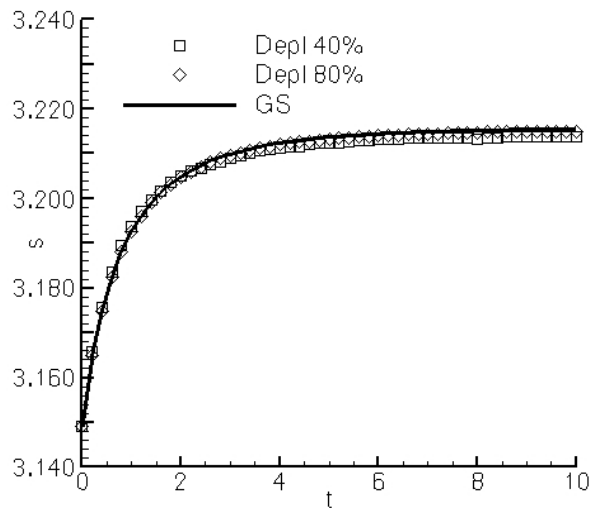


Figure 4.1.6. The entropy evolution without ensemble averaging for solutions generated with 40% and 80% depleting fractions.

The slight difference between the entropy in Gold Standard and the 80% depletion fraction calculation can be accounted for by statistical noise in the replenishing steps, using 4 replenishing pairs vs. 10, as well as the depleting step.

In addition to increasing the depleting fraction to reduce the noise, one can also change how many replenishing pairs are used: four were used here. The noise associated with the replenishing integral is highly dependent on the depleting fraction because the depleting fraction determines how much mass must be depleted, and consequently replenished, with each collision partner. As the depleting fraction decreases, the number of replenishing pairs becomes increasingly important. Consider now the time evolution of a Maxwellian distribution with a fixed depleting fraction of 40% and 1, 4, and 8 replenishing pairs. A Maxwellian should remain Maxwellian, but statistical fluctuations are introduced by the evaluation of the collision integral. The gold standard for this set of plots was generated by using the N^2 method with 10 replenishing pairs and then ensemble averaging 200 independent runs. Instantaneous slices of the distribution are plotted in figure 4.1.7 for different numbers of replenishing pairs.

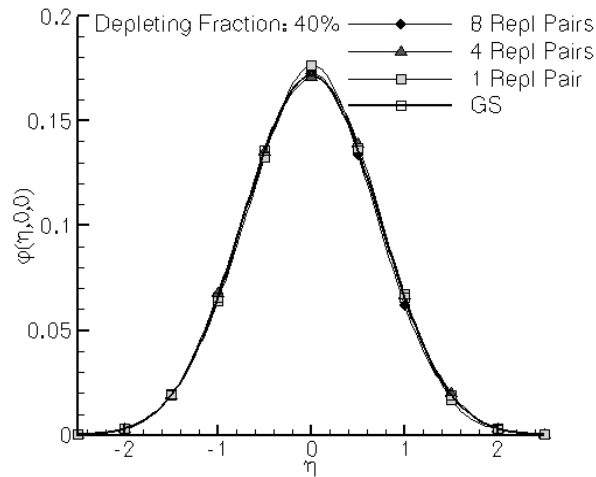


Figure 4.1.7. Slices of a Maxwellian distribution generated with different numbers of replenishing pairs.

Changing the number of replenishing pairs from 1 pair to 8 pairs does not seem to make a significant difference to the profile. With only one replenishing pair, instantaneously there is a slight overshoot at the center of the distribution but at other realizations the center of the distribution undershoots. To evaluate the noise, the entropy and RMS are also plotted for various numbers of replenishing pairs in figures 4.1.8 and 4.1.9.

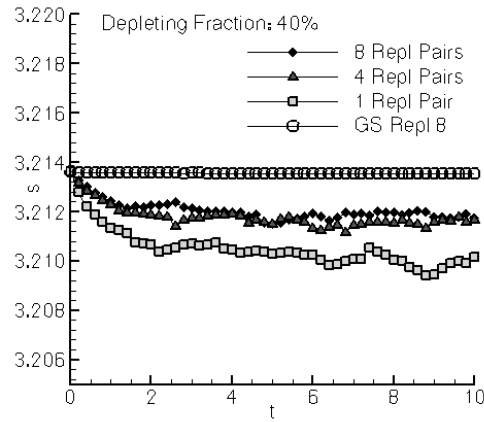


Figure 4.1.8. Entropy evolution of a Maxwellian distribution for various numbers of replenishing pairs per collision.

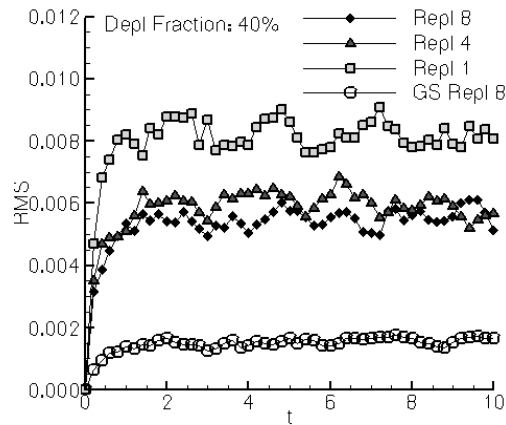


Figure 4.1.9. RMS between the GS solution and solutions computed with various replenishing pairs per collision.

Although small, the GS method still has statistical noise due to the replenishing integral and this noise is also plotted as a reference. For a depleting fraction of 40%, increasing the number of replenishing pairs from 1 to 4 reduces noise and improves accuracy of the calculated entropy, but accuracy is not greatly improved by using 8 replenishing pairs instead of 4. The decrease of error when replenishing to 4 pairs instead of 1 pair results from a smoother distribution of the replenished mass, i.e. a more accurate evaluation of the replenishing term in the collision integral. However, after a certain point, further refinement of the replenishing integral does not help much because the error mostly arises from the depleting integral. To optimize the scheme, it is important to match the errors associated with the replenishing and depleting steps.

To characterize the performance of the scheme, we relax a Maxwellian distribution for many different depleting and replenishing configurations and look at the computational time and RMS. The RMS is normalized by the peak value of the distribution function.

Figure 4.1.10 shows the mean RMS plotted against computational time for both methods. Numbers of replenishing pairs ranging from 1 to 10 were used with the N^2 method. Depleting fractions between 1% and 90% and replenishing pairs between 1 and 10 were used with the new scheme.

When plotted on a logarithmic scale, both schemes show the same rate of convergence. To reduce the error by an order of magnitude, computational time must increase by two orders of magnitude. It is impossible to reduce the computational time of the N^2 method below the time for computing with one replenishing pair. With the new method, it is possible to run much quicker at the expense of increased noise in the distribution function. Integration tends to smooth out the statistical fluctuations when

calculating physical properties such as the number density and temperature, resulting in smoother macroscopic properties.

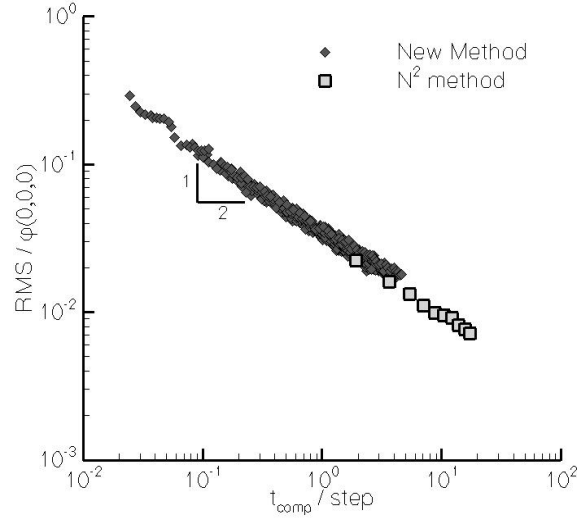


Figure 4.1.10. Rate of convergence by varying the depleting fraction and number of replenishing pairs.

The studies above were performed on a 11^3 grid with a scaled velocity spacing of 0.5 and scaled time step of 0.2. If the time step is decreased, the amount of mass moved as a result of the collision also decreases since:

$$\Delta\phi_{IJK}^{Depleting} = \Delta t \phi_{IJK} n \quad 4.1.2$$

Consequently, if the time step is very small the amount of mass distributed per collision is small and a smaller depleting fraction can be used. This becomes increasingly important when coupled with the convection step because stability of the convection routine requires a sufficiently small time step, see chapter 3 section 3. For example, in a 1D shock calculation, the scaled time step can be limited to than 0.1. For this smaller time step, a 5% depleting fraction produces less noise than with a time step of 0.2. In cases previously presented, the depleting fraction is a fixed parameter but this is in general not a requirement. The depleting fraction at a point ϕ_{IJK} can be made

proportional to the amount of mass at ϕ_{ijk} . For grid points where the distribution function is small, there is little mass and consequently collisions have a relatively small effect making a smaller depleting fraction desirable. Near the mean velocity, where the distribution function is usually largest, collisions cause relatively more mass to be shuffled and consequently a larger depleting fraction is appropriate. To improve the efficiency, a variable depleting fraction, DF, is used, where the depleting fraction varies linearly from a minimum depleting fraction at $|\phi|_{\min}$ to a maximum depleting fraction at $|\phi|_{\max}$.

$$DF(\eta_i) = DF_{\min} + \frac{|\phi(\eta_i)|}{\phi_{\max}} (DF_{\max} - DF_{\min}) \quad 4.1.3$$

Figure 4.1.11 shows a plot of minimum depleting fraction and maximum depleting fraction contoured by the CPU time per step and line contoured by the RMS.

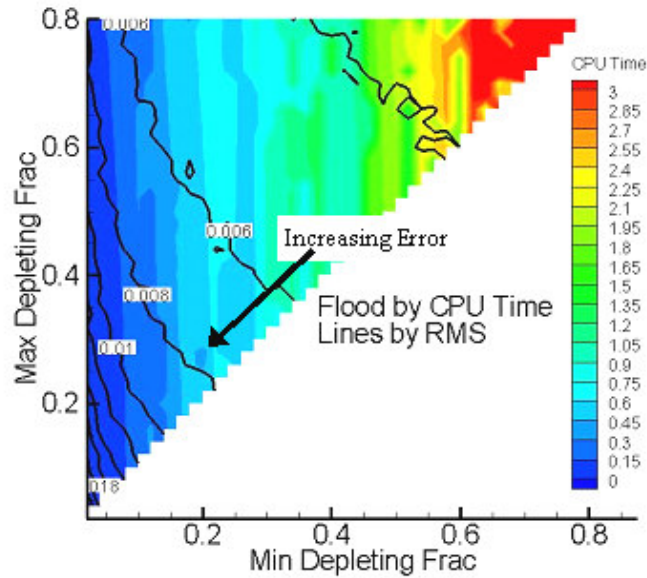


Figure 4.1.11. Contour plot for a variable depleting fraction described by equation 4.1.3. CPU time is the time per collision step and is color contoured and the rms error in the distribution is contoured by lines.

Figure 4.1.11 shows that accurate results can be obtained more efficiently using a variable depleting fraction than with a fixed depleting fraction. For example, it is possible to achieve the same error for 20% of the computational cost by using a depleting fraction that varies from 10% to 75% instead of a fixed depleting fraction of 40%.

Section 2: Different Grid Resolutions

When creating a grid in velocity space, both the range as well as the velocity spacing are important parameters. To determine whether the velocity domain extends far enough, it is not sufficient to simply truncate where the distribution goes to zero. It is also important to show that the higher physical moments are computed accurately. For example, if the integrand in the 2nd moment does not go to zero near the fringes, then the computed temperature will undershoot. Figure 4.2.1 shows a slice of the distribution function and the corresponding integrand of the 2nd moment. The velocity domain extends to $\pm 2.5\hat{T}^{1/2}$. The k^{th} moment of the distribution function is given by:

$$Q^k = \frac{1}{\hat{n}} \sum_{ijk} \left| \hat{\eta}_i - \hat{u}_i \right|^k \hat{\phi}_{ijk} \hat{\beta}_v^3 \quad 4.2.1$$

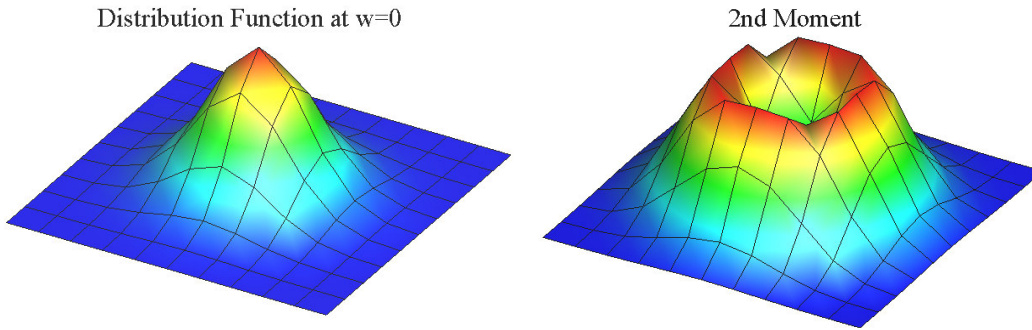


Figure 4.2.1. Planar slices of the integrands in the zeroth and 2nd moments of the Maxwellian distribution function. The velocity domain extends to ± 2.5 .

In order to resolve the higher moments, the velocity space must be larger. Fortunately, it is not important to resolve the very high moments because those have no physical

significance. The heat flux is proportional to the 3rd moment of the distribution and the 4th moment has no known physical meaning. When the velocity domain extends to $\pm 2.5\hat{T}^{1/2}$, the integrand in fourth moment does not go to zero at the edge of the domain, figure 4.2.2.

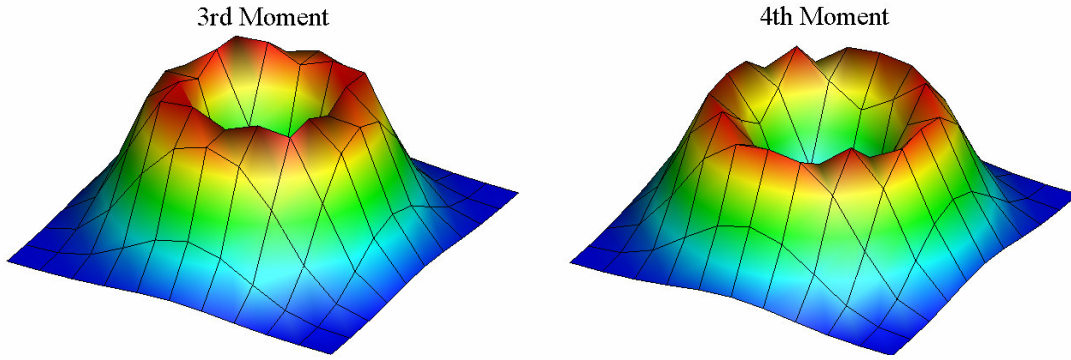


Figure 4.2.2. Planar slice of the 4th moment of a Maxwellian distribution. The velocity domain extends to ± 2.5 .

The scaled velocity spacing affects the error associated with the specific Reimann sum numerical integration routine and it limits how many velocities a discrete velocity gas must have. For practical problems, it is important to have a relatively coarse discretization in order to be computationally efficient. The velocity distribution is initialized by evaluating a continuous Maxwellian with an input density, temperature, and velocity at each discrete point in velocity space. Due to errors in numerical integration, the calculated moments from the discrete distribution are not the same as the moments of the continuous distribution. Figure 2.2.3 shows several moments of the discrete distribution function scaled by the corresponding moments of the continuous distribution function and plotted for a range of velocity spacings. Each of the moments diverges significantly from the continuous function when the scaled velocity spacing exceeds the mean thermal speed.

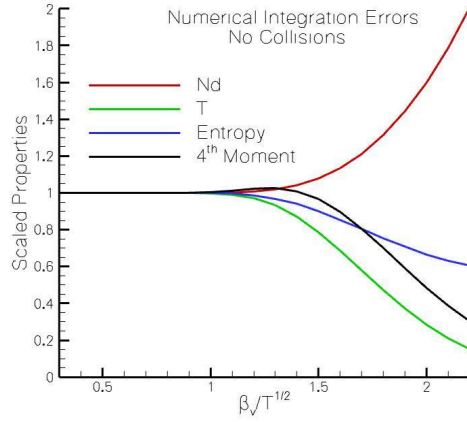


Figure 4.2.3. Numerical integration errors in density, temperature, entropy, and the 4th moment. The properties are scaled by the analytic values.

The above figure shows only the errors associated with numerical integration because the moments were calculated before collisions occur. However, once collisions are turned on errors associated with having a limited number of velocities enter the solution. In figure 4.2.4 the entropy of a relaxed discrete distribution is compared to the computed entropy before collisions are turned on.

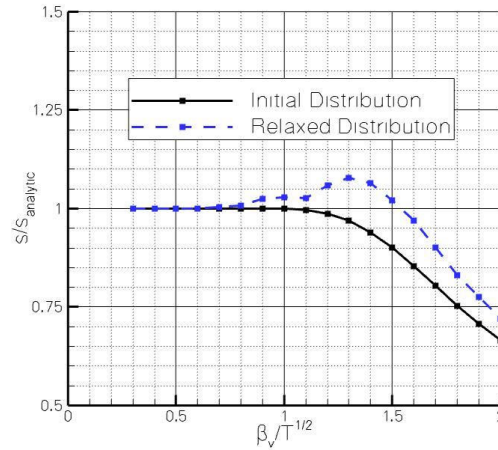


Figure 4.2.4. The error in entropy plotted for a relaxed distribution for various velocity spacings.

The relaxed distribution was generated by ensemble averaging to ensure smooth solutions, decoupling the errors caused by statistical noise. Once collisions are turned on, the entropy departs from the analytic value near a scaled velocity spacing of 0.7. Since the collision routine is conservative, the density, temperature, and velocity are conserved for all velocity spacings. Figure 4.2.5 shows the convergence of the 4th moment. In order to properly resolve the 4th moment, the scaled velocity needs to be less than half the mean thermal speed of the gas.

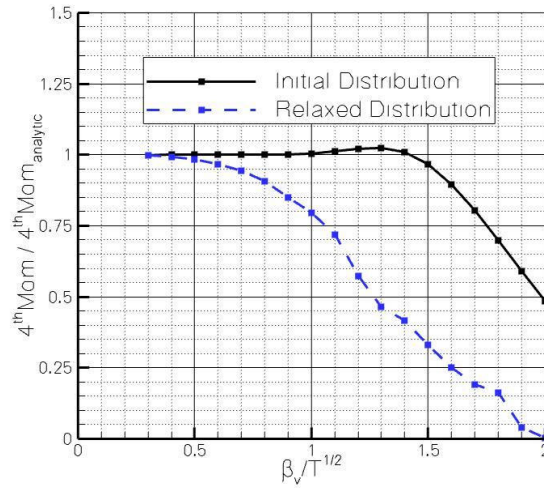


Figure 4.2.5. The error in the 4th moment plotted for various grid spacings

The departure of the higher moments from the analytic values when collisions are active is not completely understood. When the distribution function is coarse, post-collision velocities are more likely to lie farther from a grid point. Consequently, the interpolation equations may be introducing errors by mapping to points that are further away.

Section 3: Solution of the Reflected Shock

In this section the results of the numerical solution of the Boltzmann equation for a moving shock are discussed.

PROBLEM STATEMENT

To generate the shock, a gas initially moving left, figure 4.3.1, is brought to rest by a specular wall. A shock forms at the wall and propagates upstream, bringing the flow to rest while increasing the temperature and density. At the right boundary, the distribution function is set by a zero flux boundary condition.

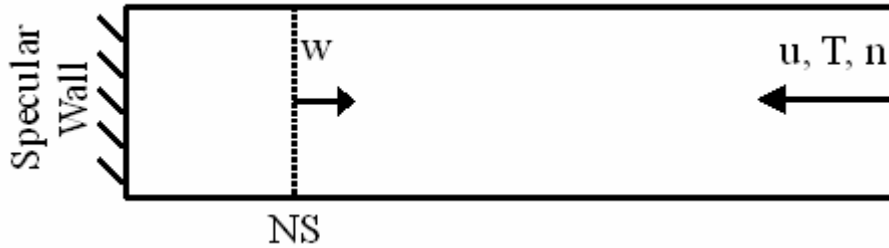


Figure 4.3.1. 1D traveling shock schematic. The shock forms by reflection off the specular wall.

In order to assess the accuracy of the numerical solution, comparisons to analytic values can be made outside of the shock. Comparisons are made to DSMC inside the shock. Jump conditions for density, pressure, and temperature across the shock, are determined by the Rankine-Hugoniot equations (see chapter 2 section 3) and the shock speed is determined from continuum dynamics. The internal shock structure depends on molecular cross sections and pseudo Maxwell molecules are used. The shock thickness δ , shown in figure 4.3.2, is defined by the maximum slope thickness based on the density. In addition to the shock thickness, the density jump lags behind the temperature shock and the corresponding separation distance, s , is also evaluated.

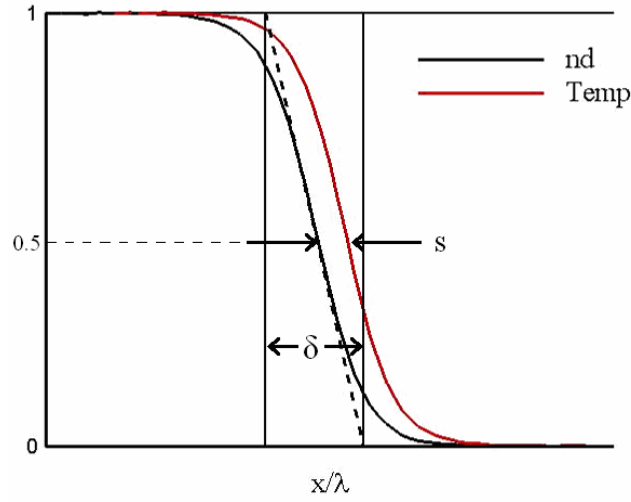


Figure 4.3.2. A schematic showing different parameters to quantify the internal shock structure.

NUMERICAL RESULTS:

Initial results were generated using a scaled velocity spacing of 0.5 spanning $\pm 4\eta_r$. The upstream scaled density and temperature are 1.0 and the initial scaled velocity is -1.0 . These conditions create a reflected Mach 1.97 shock. The time step and physical spacing are limited by the CFL condition,

$$\frac{\Delta \hat{t}}{\alpha} |\hat{\eta}_{\max}| < 1 \quad 4.3.1$$

where α is $\Delta x / \lambda_{up}$ and $\Delta \hat{t}$ is the time step scaled by the mean collision time. In general, the physical spacing should be less than the mean free path, and α was set to 0.5 for the following calculations. With this scaled space step and a maximum scaled velocity of 4, the time step is limited to less than 0.12 and in the following calculation a time step of 0.05 was used. Since the goal is to understand the limitations and performance of the collision steps, a small time step was used to minimize errors associated with convective time discretization.

Three different snapshots are plotted in figure 4.3.3 showing the density and temperature when the shock first forms, is fully developed, and at an intermediate position. The density and temperature are scaled by the Rankine-Hugoniot jump conditions, (Chapter 3.3). A variable depleting fraction, (see Chapter 4.2), ranging linearly from 10% to 60% and 2 replenishing pairs were used in the computation of the collision integral. The Rankine-Hugoniot jump conditions are recovered to within 1%.

$$\rho^* = \frac{\rho - \rho_{up}}{\Delta \rho_{R.H.}} \quad 4.3.2$$

$$T^* = \frac{T - T_{up}}{\Delta T_{R.H.}} \quad 4.3.3$$

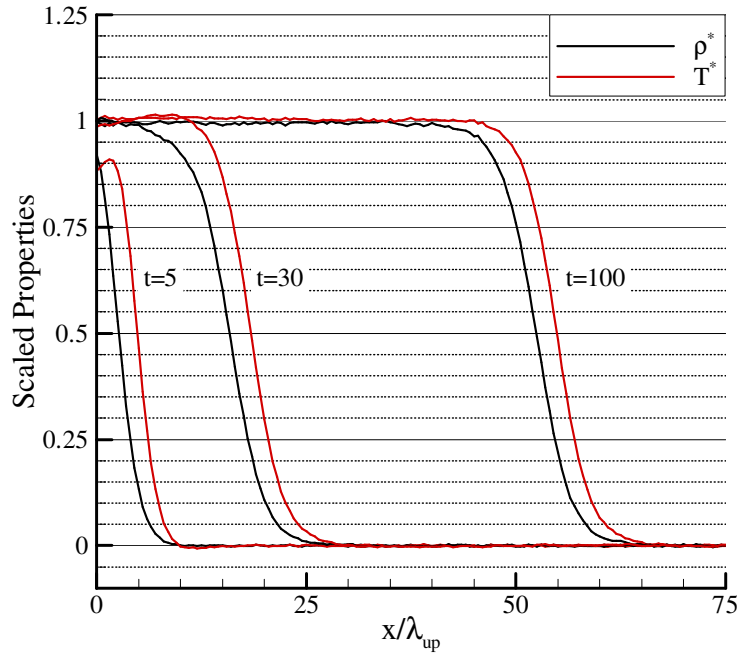


Figure 4.3.3. Mach 1.97 shock profiles when the shock first forms ($\hat{t}=5$), when the shock is fully developed ($\hat{t}=100$), and an intermediate position ($\hat{t}=30$).

The non-equilibrium induced by the specular wall by the sudden reflection at $\hat{t} = 0^+$ affects the solution until the shock moves about 25 upstream mean free paths from the wall. Near the wall, there are slightly larger variations from the Rankine-Hugoniot jump conditions. After a scaled time of 30, the shock is still near the wall and the profile is not quite symmetric. At this location, the temperature leads the density more on the downstream half of the shock than the upstream half of the shock. After the shock passes 25 mean free paths from the wall, the shock shape asymptotes to a constant value. For this Mach 1.97 shock, the maximal density gradient shock thickness is 8.2 upstream mean free paths.

In addition to the temperature and density, it is also interesting to plot the higher moments of the distribution in figure 4.3.4.

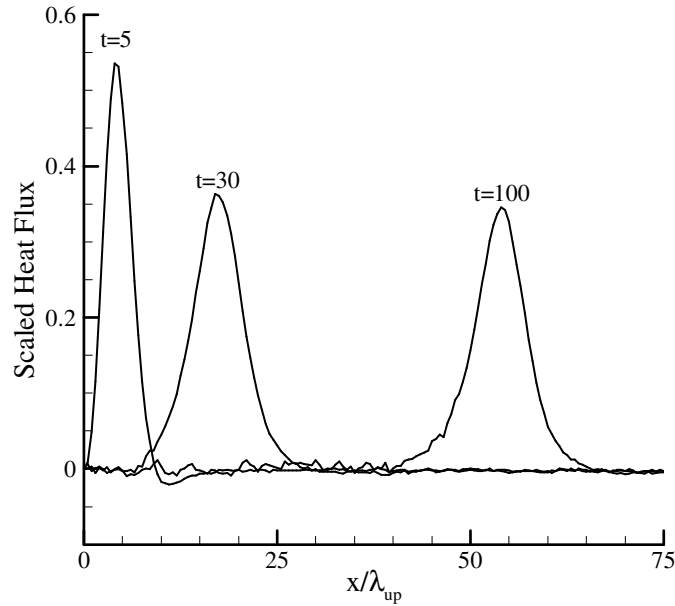


Figure 4.3.4. Snapshots of the scaled heat flux for a Mach 1.97 shock.

When the shock first forms, there is a peak in the heat flux corresponding to the instantaneous temperature rise imposed by the specular boundary condition. However,

once the shock propagates about 25 mean free paths away from the wall, the maximum heat flux inside of the shock asymptotes to a constant value. At a scaled time of 5, when the shock is still close to the wall, the heat flux is slightly negative on the upstream side of the shock. The undershoot tends to occur regardless of how finely the collision integral is approximated. This phenomenon vanishes after the shock moves sufficiently far from the wall, implying that the specular wall causes the disturbance. In addition, the computed heat flux upstream of the shock has less statistical noise than the computed heat flux downstream.

In figure 4.3.5, slices of the distribution are plotted upstream, downstream, and inside of the shock.

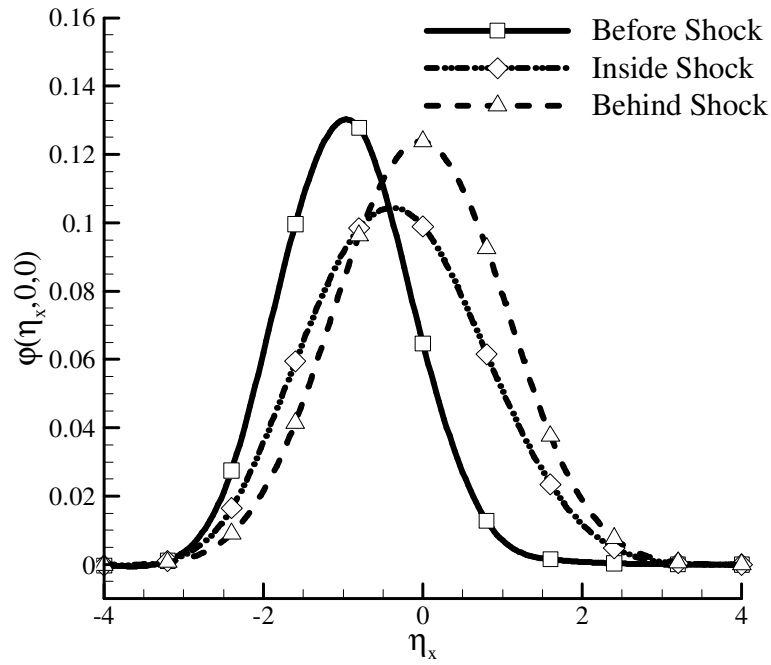


Figure 4.3.5. Slices of the distribution along the x-velocity axis downstream, upstream, and inside the shock. The symbols are the lattice sites.

Ahead of the shock, the distribution function is moving to the left with a mean velocity of -1.0 . As the shock forms, the mean velocity shifts towards the right and the distribution becomes shorter and wider. Midway through the shock, the distribution function becomes taller and widens. In all three cases, the tails of the distribution go to zero at the edge of the domain.

VELOCITY GRID RESOLUTION

For efficient calculations, the velocity domain must be relatively coarse and understanding the limits is important for optimizing the scheme. Four velocity grids with different resolutions are used to solve a traveling Mach 1.97 shock. Each velocity grid tested extends to $\pm 4\eta_r$, but the scaled velocity spacing is varied from 0.67 to 1.33. A variable depleting fraction ranging from 1% to 10% was used along with two replenishing pairs per collision for each calculation.

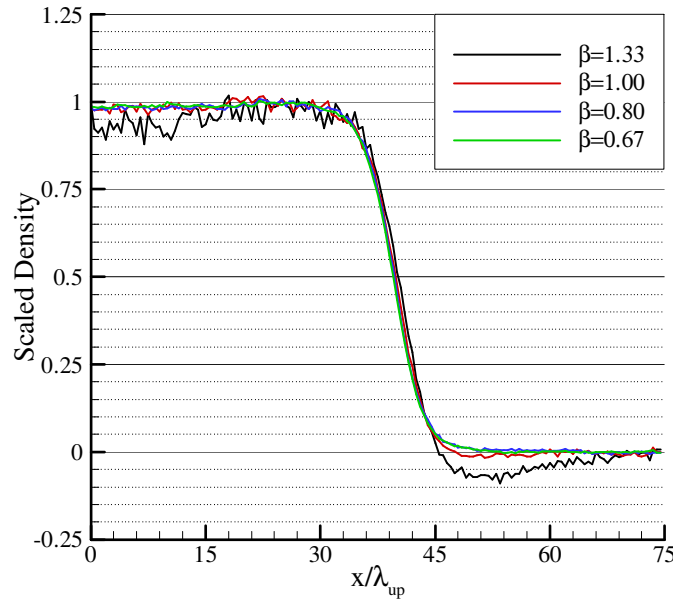


Figure 4.3.6. Mach 1.97 shock profiles generated with velocity grids of varying resolutions.

In figure 4.3.6, the density is plotted at a scaled time of 75. At this time, the shock is far enough from the wall so that boundary effects are confined near the wall and not seen in the shock wave. All four solutions show relatively good agreement on the shock position, showing that the computed shock speed is not affected by the discretization. The density profiles for the higher resolution velocity grids with a scaled spacing of 0.67 and 0.8 agree very well. When the scaled velocity spacing is further increased to 1.0, the density starts to undershoot slightly upstream of the shock. When the scaled velocity spacing is further increased, the density undershoot increases. Additionally, the fluctuations near the wall tend to be larger when a coarser grid is used.

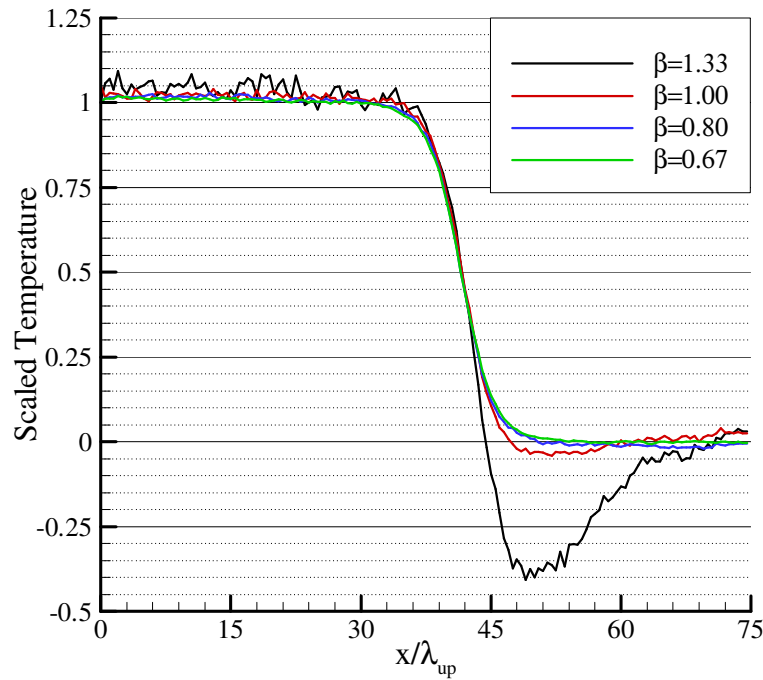


Figure 4.3.7. Mach 1.97 temperature profiles computed with velocity grids of varying resolutions.

The temperature is more sensitive to the grid resolution than the density, and corresponding temperature profiles are shown in figure 4.3.7. Similar to the number

density, the temperature undershoots upstream of the shock when the scaled velocity spacing $\beta \geq 1.0$. When $\beta > 1.0$, large errors are expected due to error in numerical integration (Section 4.2). In figure 4.3.8, slices of the distribution are plotted for coarse and fine grid resolutions immediately upstream of the shock and behind the shock. The profiles are vastly different suggesting that the undershoot can not be attributed solely to errors in numerical integration. When the velocity spacing exceeds a certain threshold, too much mass is depleted from the center of the distribution function.

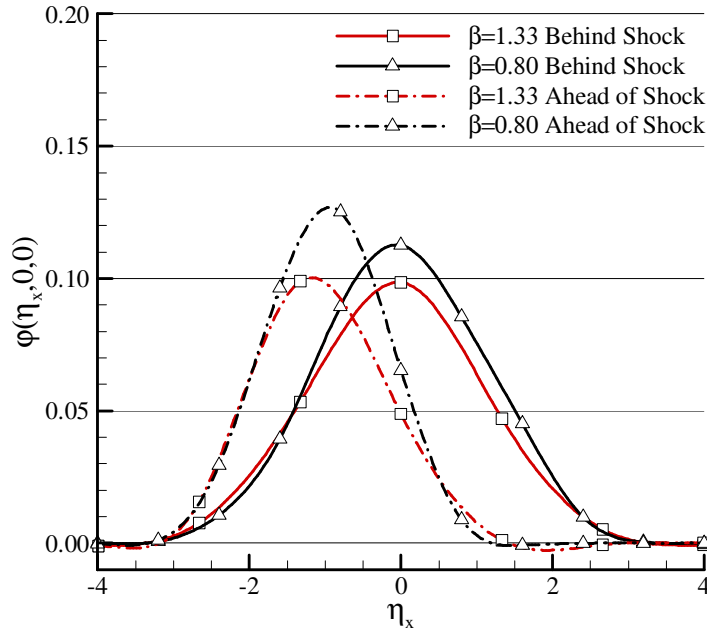


Figure 4.3.8. Slices of the distribution function immediately ahead and downstream of a Mach 1.97 shock. The symbols correspond to lattice sites.

Different depleting fractions are used to see if the undershoot is related to the coarseness in evaluating the collision integral. Temperature profiles generated via depleting fractions of 1% and 60% and a grid with a scaled velocity spacing of 1.0 are plotted in figure 4.3.8.

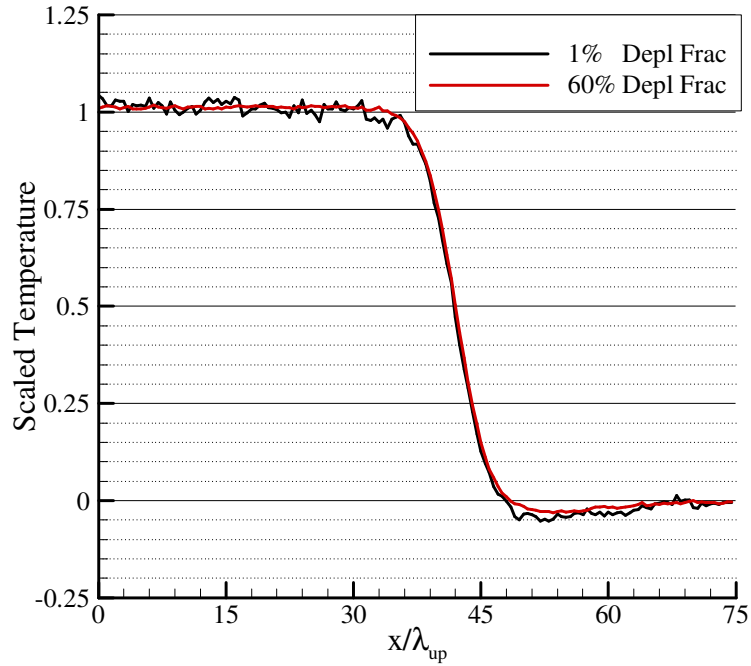


Figure 4.3.8. Mach 1.97 temperature profile obtained with a scaled velocity spacing of 1.0 and depleting fractions of 1% and 60%.

Although the noise is reduced as the depleting fraction is increased to 60%, the temperature continues to undershoot upstream of the shock. Comparisons are not made to the N^2 method because even with a coarse velocity discretization the N^2 method requires several weeks to obtain a solution. The only way to prevent this is to improve the resolution such that the scaled velocity spacing is less than 1.0.

INTERNAL SHOCK STRUCTURE

The flow is not in equilibrium inside the shock wave and the shock structure depends on how the gas equilibrates. In general, the quicker the gas equilibrates, the thinner the shock wave. Comparisons of the internal shock structure are made to DSMC for three different cases: a Mach 1.97 shock wave, a weak Mach 1.2 shock wave, and a

stronger Mach 6 shock wave. The DSMC solutions are generated using Bird's DSMC1S code [1] originally presented in 1988 and more recently updated in 1994.

In figure 4.3.9 a Mach 1.97 traveling shock computed by the discrete velocity model is compared to a stationary Mach 1.97 computed by DSMC. The traveling shock wave profile was taken when the shock was 70 mean free paths from the wall. A velocity space spanning to $\pm 4\eta_r$ with a scaled velocity spacing of 0.8 was used. A time step $\Delta\hat{t} = 0.05$ and a scaled physical spacing $\alpha = 0.5$ were used and the computational time required to perform 2000 time steps on 200 points was 2870 seconds. A depleting fraction ranging from 0.01 to 0.1 was used along with 2 replenishing pairs per collision.

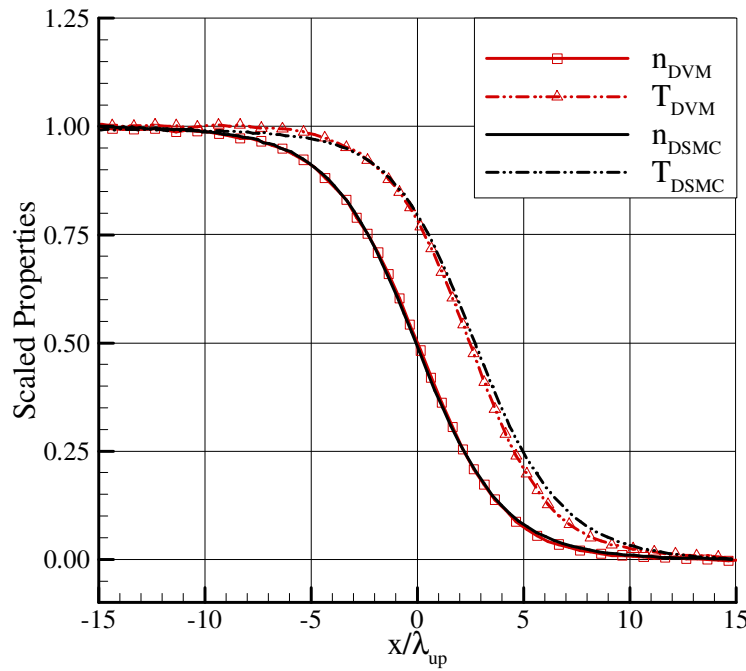


Figure 4.3.9. Mach 1.97 shock profiles comparing discrete velocity solutions to DSMC solutions.

The density profile matches the DSMC solution very closely on both the upstream and downstream halves of the shock. The corresponding shock thickness measured by

the maximum density gradient is 8.2 upstream mean free paths. On the downstream half of the shock, the temperature profile closely matches the DSMC. On the upstream side of the shock, the discrete velocity temperature profile lags slightly behind the DSMC profile. The shift between the temperature and density computed with the discrete velocity model is 2.4 mean free paths where the shift computed with DSMC is 2.6 mean free paths. As the Mach number is decreased the shock thickness becomes increasingly large and the jump conditions across the shock wave decrease.

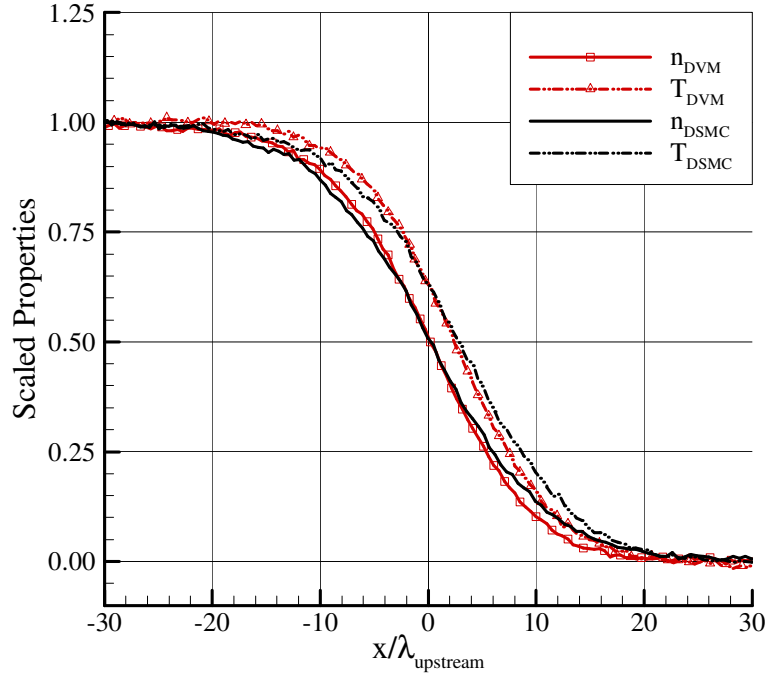


Figure 4.3.10. Mach 1.2 shock profiles comparing discrete velocity and DSMC solutions.

Figure 4.3.10 shows the results of a weak shock (Mach 1.20) calculation. The statistical fluctuations are more noticeable than the higher Mach number cases because the jump conditions across a weak shock are very small and nearly on the same order as the statistical fluctuations. To obtain a smooth DSMC profile, 10 million simulated

particles were used along with 200 cells in physical space. As expected the shock thickness is much larger for a low Mach number compared to the higher Mach number cases. A variable depleting fraction ranging from 10% to 60% was used in the discrete velocity model. A time step of 0.05 and physical spacing of $0.5\lambda_{upstream}$ were used and the physical domain was generated using 200 physical cells. The shock was allowed to propagate for 2000 time steps and the profile was captured at time $\hat{t} = 100$. Using the above conditions, the DVM solution required 208 minutes. At a low Mach number of 1.2 the Rankine-Hugoniot conditions are satisfied, but there are slight differences between the DSMC solution and the DVM solution. The DSMC shock wave is thicker than the discrete velocity shock wave and the difference is more evident at lower Mach numbers than higher Mach numbers. As the Mach number is decreased below 1.25, the shock wave thickness increases rapidly [1]. If the Mach numbers for the DSMC and DVM cases do not match very closely because of discretization errors, the shock thicknesses may be noticeably different. Although the DSMC profile was generated with 10 million molecules, there is still noise in the solution. The DSMC code attempts to keep the shock stationary by slightly adjusting the downstream boundary conditions, but for solutions with statistical noise the shock wave may wander slightly. If the shock wave oscillates slightly, the shock wave profile will smear because of the ensemble averaging. For higher Mach number cases, there are a wide range of velocities and very high temperatures exist downstream of the shock wave.

To generate a Mach 6 shock, figure 4.3.12 the velocity domain must be very large because the temperature increases by a factor of 12 and the corresponding downstream distribution function is relatively wide and flat. In addition to needing a large velocity domain, the resolution has to be sufficient to resolve the cold and narrow upstream distribution function. Numerical tests have shown that in order to avoid large truncation

errors downstream of the shock wave, the velocity domain must extend to $\pm 2.5\eta_r T^{1/2}$. The scaled velocity spacing needs to be less than $1.0T^{1/2}$ to resolve the profile upstream of the shock wave. For a Mach 6 shock, the velocity domain extends to $\pm 11.4\eta_r$ and the scaled velocity spacing is 0.95. The resulting velocity space contains 15625 points and the corresponding computational costs are very large. A very low depleting fraction ranging from 0.01 to 0.05 was used along with 2 replenishing pairs per collision. The computational time required to perform 1200 time steps on 100 points in physical space was 12.1 hours.

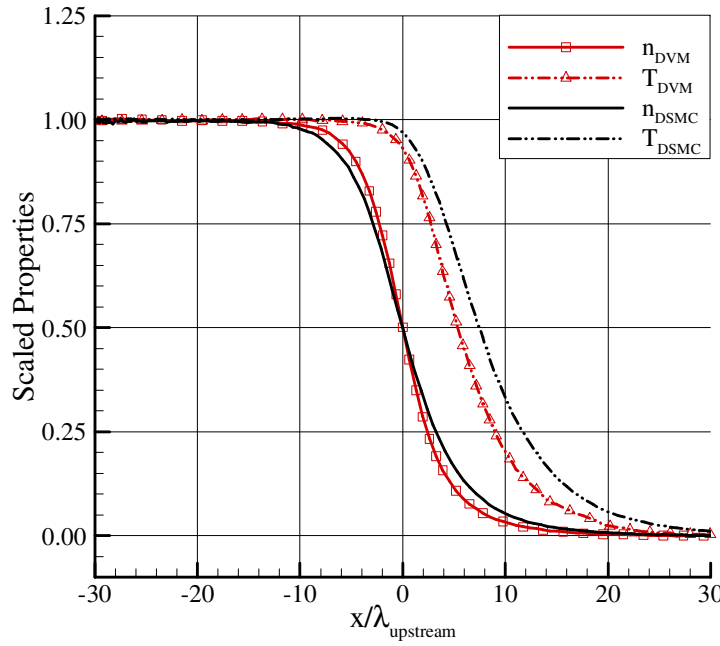


Figure 4.3.11. Mach 6.01 shock profiles comparing discrete velocity and DSMC solutions.

In figure 4.3.11, the shock thickness computed by the discrete velocity model is $9.5\lambda_{upstream}$, which is slightly thinner than the $13.0\lambda_{upstream}$ shock thickness computed by DSMC. Additionally, the separation distance between the density and temperature waves

computed by the discrete velocity is 1.75 mean free paths less than the separation computed with DSMC.

Relatively good agreement between DSMC and the discrete velocity model has been obtained for Mach 1.97 shock waves, but at higher Mach numbers the waves computed with the discrete velocity model tend to be steeper than the profiles generated with DSMC. To find the source of the discrepancy, the time step, physical spacing, resolution in velocity space, range of velocity space, and depleting fractions have been adjusted with little success in exactly matching the DSMC profile. The differences are consistent with those presented by the Δ - ε method (Tan, 1991) where at higher Mach numbers discrepancies in the temperature profiles were also found.

COST COMPARISON

To evaluate the performance, the time required to generate a solution with a certain level of noise is compared for the discrete velocity and DSMC solutions. In all cases previously presented, the DSMC solutions required less time than the discrete velocity model. However, this is not a direct comparison because the DSMC solution was for a steady shock wave and the discrete velocity model was applied to a traveling shock wave. Since the DSMC code generates a steady shock wave, time averaging is used to rapidly obtain smooth profiles where averaging is not used with the discrete velocity model. For a direct comparison of the computational costs, the discrete velocity model was adapted to a steady shock wave and the averaging procedure in the DSMC code was turned off. Ensemble averaging was not used to characterize the performance in both the DSMC and discrete velocity calculations because for unsteady problems ensemble averaging may not be permissible.

To generate a steady shock wave the right half of the physical domain was initialized to the upstream flow conditions and the downstream half of the physical

domain was set to the corresponding Rankine-Hugoniot conditions. A zero flux boundary condition was imposed at both the upstream and downstream boundaries. Using the updated boundary and initial conditions, a steady Mach 1.97 shock wave was used to compare the computational performance between the discrete velocity and DSMC models.

All simulations were performed on a desktop computer with an Intel 2.4GHz processor, 4GB of RAM, and a 2MB cache. The noise was evaluated by computing the RMS, eq 4.4.1, in sections downstream and upstream of the shock wave that were at least 20 physical cells away from the boundaries and sufficiently far from the shock.

$$RMS = \sqrt{\frac{1}{N_s} \sum_{i=1}^{N_s} (n_i - \bar{n})^2} \quad 4.4.1$$

In both the DSMC and discrete velocity simulations, 200 physical cells with a scaled physical spacing $\alpha = 0.5$ and a time step $\Delta \hat{t} = 0.05$ were used. After a steady shock developed, the simulation continued to run for an additional 1500 time steps and the corresponding computational time was recorded. To evaluate the rate of convergence, the DSMC simulation was performed 10 times by varying the numbers of computational molecules. The discrete velocity simulation was executed 14 times with different depleting fractions and a fixed 2 replenishing pairs per collision. A linearly varying depleting fraction, equation 4.1.3, was used and this was adjusted by keeping the lower bound fixed at 1% and changing only the upper bound from 5% to 70%.

Figure 4.4.1 shows the noise in the density upstream and downstream of the shock wave plotted against the corresponding computational time per time step.

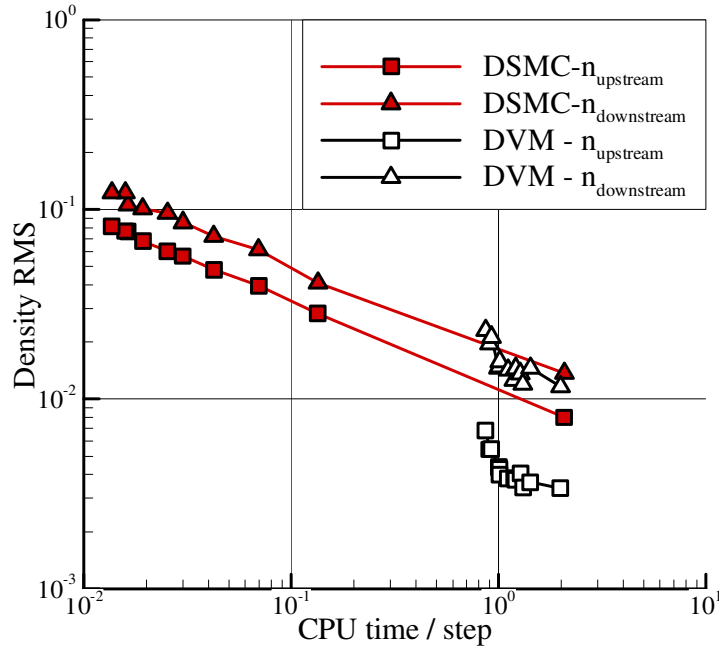


Figure 4.4.1. Noise in the density upstream (squares) and downstream (triangles) of the shock wave plotted against the computational time for discrete velocity and DSMC solutions.

In both the DSMC and DVM (discrete velocity model) computations, the noise is less on the upstream side of the shock than the downstream half. This may occur because the flow upstream of the shock is supersonic and the noise largely does not propagate upstream, whereas downstream of the shock wave the flow is subsonic and fluctuations can propagate upstream. The discrete velocity model performs better than DSMC upstream of the shock wave. For a smooth upstream solution with noise less than 0.004, the DVM is approximately an order of magnitude quicker than DSMC. Downstream of the shock wave, the differences between DSMC and the DVM are subtle, with only marginal improvements to the performance. DSMC performs better downstream of the shock wave because the downstream density is higher and consequently more

computational molecules are present in the downstream region. Similarly, upstream of the shock wave the density is lower and there are fewer computational molecules to sample from. In the discrete velocity model, there are not particles and consequently the lower density downstream does not adversely affect the noise level.

The cost comparisons above only address the affect of varying the depleting fraction, but there exist other ways to modify how accurately the collision integral is computed. In addition to the depleting fraction, number of replenishing pairs, time step, physical spacing, velocity spacing, and the range of the velocity space can also affect the computational performance. The parameter space becomes more complicated when a varying depleting fraction is used instead of a fixed depleting fraction. Consequently, there are many other parameters that have not been examined in a performance study that can change the computational efficiency. Modifications to only the depleting fraction were used because from experience it has a larger affect on how accurately the collision integral is computed.

CHAPTER 5: CONCLUSIONS

Summary of Key Points

Investigation of a discrete velocity model was motivated by the need for a Boltzmann equation solver that can be applied to unsteady flows that bridge the rarefied and continuum regimes. In this regime the flows are non-equilibrium and highly collisional and consequently it is computationally expensive to obtain smooth transient data. The key features of the proposed discrete velocity method are:

- Interpolation algorithm was developed to allow for arbitrary post-collision velocities.
- The computational cost was reduced by statistically evaluating the collision integral.
- Homogeneous relaxation results agree well with analytic results for relaxation of the Bobylev Krook Wu distribution.
- 1D results for traveling shock waves agree well with DSMC solutions.

INTERPOLATION SCHEME

In traditional discrete velocity models, the post collision velocities are restricted to those that lie precisely on the grid. This can artificially limit the number of collisions and consequently affect the rate at which the gas equilibrates. To solve this problem, an interpolation scheme was developed that maps points that lie off the grid onto a stencil of grid points that surrounds the point to be interpolated. Since elastic collisions preserve mass, momentum, and energy, the interpolation scheme was designed to also preserve those quantities. This interpolation routine allows the discrete velocity scheme to permit post-collision velocities that lie between grid points or entirely outside of the velocity domain. In order to satisfy the conservation equations, the interpolation depletes mass from ‘external points’ of a several point stencil. If the ‘external’ points do not have

enough mass to accommodate the depletion, the distribution function can go negative. ‘Sweeping’ algorithms have been developed to remove the negative values, but this is only performed to evaluate the entropy. In general, the negative values are not a problem because the distribution function only goes negative near the fringes and the magnitude of these negative values is very small.

STATISTICAL EVALUATION OF THE COLLISION INTEGRAL

The collision integral can be accurately evaluated by considering collisions between each point in velocity space with all other points in velocity space. This is computationally expensive, $O(N_v^2)$. To reduce the computational cost, the collision integral is solved statistically by colliding each point in velocity space with a handful of randomly selected collision partners. The collision partners are selected via an algorithm that biases points that contribute more to the collision integral. To reduce the computational cost associated with an acceptance-rejection, a new selection scheme was implemented that selects collision partners that contribute more to the collision integral with only one random number call. It was found that relatively smooth solutions for the macroscopic variables of interest can be obtained using a relatively small set of randomly chosen collision partners. Further improvements were made by using a varying depleting fraction. For collisions that result in small changes to the collision integral a small depleting fraction was used. The numerical scheme was then applied to homogeneous and one dimensional problems.

HOMOGENEOUS RESULTS

The scheme was first applied to homogeneous relaxation problems to test the collision routine. The two test problems analyzed were relaxation of a Maxwellian distribution and relaxation of the Bobylev-Krook-Wu distribution. The collision routine

was shown to preserve the Maxwellian distribution and conserved mass, momentum, and energy. The Bobylev-Krook-Wu distribution has an analytic solution describing its time relaxation. Using a relatively small depleting fraction of 40%, it was found that the entropy tracks the analytic solution to within 0.1%. Although computational time can be reduced by using a depleting fraction of 5%, the entropy falls short of the analytic value. The “Gold Standard” entropy is recovered if the distribution functions generated with a 5% depleting fraction are ensemble averaged. By solving the collision integral statistically with a small depleting fraction, it is possible to increase the speed by nearly two orders of magnitudes compared to the N_v^2 method. The ability to perform collisions quicker allows for efficient calculation of 1D unsteady problems.

1D TRAVELING SHOCK RESULTS

The discrete velocity method was extended to one dimension and used to solve a traveling normal shock problem. The Rankine-Hugoniot jump conditions were recovered for shock waves ranging from Mach 1.2 to Mach 6. The velocity space was limited to scaled velocity spacings being less than $1.0\sqrt{\hat{T}_{up}}$. If the scaled velocity spacing is too large, then the density and temperature tend to undershoot upstream of the shock. The internal shock structure was compared to DSMC calculations. The DSMC solutions compared well for a Mach 1.97 shock with slight variations occurring on the upstream half of the temperature profile. There are slightly larger variations between DSMC and the new model for a stronger Mach 6 shock wave. The discrete velocity model slightly under predicts the shock thickness separation distance between the density and temperature waves. The Mach 1.2 shock wave structure closely matches the DSMC solutions, but a high accuracy solution to the collision integral is required to ensure that the statistical fluctuations are much less than the jump conditions across the weak shock wave.

Future Work

In previous discrete velocity models, the restriction of post-collision velocities limits the applicability to problems with inelastic collisions and multiple species. For inelastic collisions, the relative velocity vector can shrink or grow. Consequently, it is possible that no replenishing velocities will lie on the grid. The interpolation algorithm that maps points that lie off the grid back onto the nearby grid points can be extended to inelastic collisions.

Since the post-collision velocities are not restricted by the structure of the grid, it is now possible to use a non-uniform velocity grid. Non-uniform velocity grids have been applied to spectral models [29] and shown possible for discrete velocity models in [17], but challenges remain on how to cluster points in a non-uniform velocity grid. The interpolation scheme can also be used to transition from a coarse velocity grid to a fine velocity grid or vice versa. For example, suppose a solution to a steady high Mach number normal shock is desired. On the upstream side of the shock the distribution function will be narrow and centered about a mean velocity different than the downstream mean velocity. On the downstream side of the shock, the distribution function will be wider and centered about a different mean velocity. Since the two distributions upstream and downstream are vastly different it may be beneficial to have different velocity grids upstream and downstream of the shock.

APPENDIX A: STATISTICAL EVALUATION OF THE DEPLETING INTEGRAL

Direct evaluation of the depleting integral is computationally expensive and a statistical method is used to reduce the cost. For isotropic scattering the angular dependence can be integrated immediately and the incremental depletion at a given point $\hat{\eta}_i$ is given by

$$\Delta\hat{\phi}_{depl}(\hat{\eta}_i) = \Delta\hat{t} \int_{\hat{\zeta}_i} \hat{\phi}(\hat{\zeta}_i) \hat{\phi}(\hat{\eta}_i) \hat{g} \hat{\sigma}_T d\hat{\zeta}_i = \Delta\hat{t} \hat{\phi}(\hat{\eta}_i) \int_{\hat{\zeta}_i} \hat{\phi}(\hat{\zeta}_i) \hat{g} \hat{\sigma}_T d\hat{\zeta}_i. \quad 1$$

In a discrete gas, the integral is the sum of delta functions located at each discrete velocity. We assume a constant scaled velocity spacing β in each velocity coordinate.

$$\Delta\hat{\phi}_{depl}(\hat{\eta}_i) = \Delta\hat{t} \hat{\phi}(\hat{\eta}_i) \sum_{\hat{\zeta}_i \neq \hat{\eta}_i} \hat{\phi}(\hat{\zeta}_i) \hat{g} \hat{\sigma}_T \beta^3. \quad 2$$

If pseudo-Maxwell molecules are assumed, $\hat{g} \hat{\sigma} = 1$ and Eq. 2 simplifies to:

$$\Delta\hat{\phi}_{depl}(\hat{\eta}_i) = \Delta\hat{t} \hat{\phi}(\hat{\eta}_i) \sum_{\hat{\zeta}_i \neq \hat{\eta}_i} \hat{\phi}(\hat{\zeta}_i) \beta^3 = \Delta\hat{t} \hat{\phi}(\hat{\eta}_i) (\hat{n} - \beta^3 \hat{\phi}(\hat{\eta}_i)). \quad 3$$

Note that the depletion can be calculated explicitly at each computational step. In the proposed statistical representation, points participate in collisions in two different ways. Each point in velocity space is first chosen as a test point and collides with a set of randomly chosen field points. Secondly, the point may be randomly chosen as a field point when the depletion is computed for other velocities as test points. Half of the depletion, given by Eq. 3, should occur in each case. The goal of the statistical scheme is to ensure that Eq. 3 is satisfied on the average; i.e. the expectation values of the depletion should be half of the value given by Eq. 3 when the velocity point is a test point, and when it is a field point. In the following derivation, $\hat{\eta}$ denotes the velocity of a test point, and $\hat{\zeta}$ denotes the velocity of a randomly chosen field point.

First, consider the depletion at $\hat{\eta}$ when it is a test point colliding with field points $\hat{\zeta}$. If the velocity distribution function is positive everywhere, the incremental depletion for the test point is simply half of Eq. 3

$$\Delta\hat{\phi}_{Depl}^{half}(\hat{\eta}|\hat{\zeta}) = \frac{1}{2}\Delta\hat{t}\hat{\phi}(\hat{\eta})(\hat{n} - \hat{\phi}(\hat{\eta})\beta^3). \quad 4$$

However, negative values of the distribution are permitted in the present scheme. A single depleting collision between a velocity $\hat{\eta}$ and $\hat{\zeta}^*$ is the integrand of Eq. 1.

$$\Delta\hat{\phi}_{depl}(\hat{\eta}|\hat{\zeta}^*) = \Delta\hat{t}\hat{\phi}(\hat{\eta})\hat{\phi}(\hat{\zeta}^*)\hat{g}\hat{\sigma}. \quad 5$$

If one of the collision partners in Eq. 5 is negative, a depleting collision becomes a replenishing collision because of the negative sign. If both collision partners are negative, the negative signs cancel and the collision remains a depleting collision. Equation 4 is modified to allow for negative values and the depletion at the test point is defined by

$$\Delta\hat{\phi}_{Depl}^{half}(\hat{\eta}|\hat{\zeta}) = \frac{1}{2}\hat{\phi}(\hat{\eta})\Delta\hat{t}(\hat{n} - 2\hat{n}_{neg} - |\hat{\phi}(\hat{\eta})|\beta^3)\text{sgn}(\hat{\phi}(\hat{\zeta})), \quad 6$$

where

$$\text{sgn}(x) = \begin{cases} 1 & x \geq 0 \\ -1 & x < 0 \end{cases}. \quad 7$$

Equation 6 now depends on the sign of $\hat{\phi}(\hat{\zeta})$, e.g. if the field point is negative and the test velocity is positive, the depleting collision acts as a replenishing collision. Equation 6 can be re-written by noting that $\hat{n} - 2\hat{n}_{neg} = \sum \beta^3 |\hat{\phi}(\hat{\zeta}^*)|$

$$\Delta\hat{\phi}_{Depl}^{half}(\hat{\eta}|\hat{\zeta}) = \frac{1}{2}\hat{\phi}(\eta)\Delta\hat{t}\beta^3\left(\sum_{\zeta^* \neq \eta} |\hat{\phi}(\hat{\zeta}^*)|\right)\text{sgn}(\hat{\phi}(\hat{\zeta})). \quad 8$$

Equation 8 can be re-written as an expectation value, by replacing $\text{sgn}(\hat{\phi}(\hat{\zeta}))$ with the probability, P_{neg} , that $\hat{\phi}(\hat{\zeta})$ will be negative:

$$\begin{aligned}
\langle \Delta \hat{\phi}_{Depl}^{half}(\hat{\eta} | \hat{\zeta}) \rangle &= \frac{1}{2} \hat{\phi}(\hat{\eta}) \Delta \hat{t} \beta^3 \left(\sum_{\hat{\zeta}^* \neq \hat{\eta}} |\hat{\phi}(\hat{\zeta}^*)| \right) (-P_{neg} + (1 - P_{neg})) \\
&= \frac{1}{2} \hat{\phi}(\hat{\eta}) \Delta \hat{t} \beta^3 \left(\sum_{\hat{\zeta}^* \neq \hat{\eta}} |\hat{\phi}(\hat{\zeta}^*)| \right) (1 - 2P_{neg})
\end{aligned} \tag{9}$$

For a test point $\hat{\eta}$, the probability that the distribution function $\hat{\phi}(\hat{\zeta})$ at the randomly drawn field point is negative is:

$$P_{neg} = \begin{cases} \frac{-\hat{n}_{neg} + \hat{\phi}(\hat{\eta}) \beta^3}{\sum_{\hat{\zeta}^* \neq \hat{\eta}} |\hat{\phi}(\hat{\zeta}^*)| \beta^3} & ; \hat{\phi}(\hat{\eta}) < 0 \\ \frac{-\hat{n}_{neg}}{\sum_{\hat{\zeta}^* \neq \hat{\eta}} |\hat{\phi}(\hat{\zeta}^*)| \beta^3} & ; \hat{\phi}(\hat{\eta}) \geq 0 \end{cases} \tag{10}$$

The probability of a negative partner being drawn depends on the sign of $\hat{\phi}(\hat{\eta})$ because the test point is excluded from the set of available collision partners. Note that $\hat{n}_{neg} < 0$, so $P_{neg} > 0$.

First consider the case when $\hat{\phi}(\hat{\eta}) \geq 0$. When Eq. 10 is substituted into Eq. 9, the expectation for the depletion becomes:

$$\langle \Delta \hat{\phi}_{Depl}^{half}(\hat{\eta} | \hat{\zeta}) \rangle = \frac{1}{2} \hat{\phi}(\hat{\eta}) \Delta \hat{t} \left(2\hat{n}_{neg} + \sum |\hat{\phi}(\hat{\zeta}^*)| \beta^3 - |\hat{\phi}(\hat{\eta})| \beta^3 \right). \tag{11}$$

Simplifying and noting that $\hat{n} = 2\hat{n}_{neg} + \sum |\hat{\phi}(\hat{\zeta}^*)| \beta^3$, Eq. 11 becomes

$$\langle \Delta \hat{\phi}_{Depl}^{half}(\hat{\eta} | \hat{\zeta}) \rangle = \frac{1}{2} \hat{\phi}(\hat{\eta}) \Delta \hat{t} \left(\sum_{\hat{\zeta}^* \neq \hat{\eta}} \hat{\phi}(\hat{\zeta}^*) \beta^3 \right). \tag{12}$$

Next consider the case when $\hat{\phi}(\hat{\eta}) < 0$. When Eq. 10 is substituted into Eq. 9 the depletion becomes:

$$\Delta \hat{\phi}_{Depl}^{half}(\hat{\eta}) = \frac{1}{2} \hat{\phi}(\hat{\eta}) \Delta \hat{t} \left(2\hat{n}_{neg} + \sum |\hat{\phi}(\hat{\zeta}^*)| \beta^3 - |\hat{\phi}(\hat{\eta})| \beta^3 - 2\hat{\phi}(\hat{\eta}) \beta^3 \right) \tag{13}$$

Simplifying and noting that $\hat{\phi}(\hat{\eta}) < 0$, Eq. 13 is identical to Eq. 12. Therefore, the expectation value for the total depletion at test point $\hat{\eta}$ is:

$$\langle \Delta \hat{\phi}_{Depl}^{half}(\hat{\eta}) \rangle = \frac{1}{2} \hat{\phi}(\hat{\eta}) \Delta t \left(\sum_{\hat{\zeta}^* \neq \hat{\eta}} \beta^3 \hat{\phi}(\hat{\zeta}^*) \right) \quad 14$$

Next, consider the depletion at $\hat{\zeta}$ when it is a field point colliding with all other test points $\hat{\eta}$. In the present scheme, the probability of a point located at $\hat{\zeta}$ being among the set of M_j collision partners for a test point $\hat{\eta}$ is:

$$P(\hat{\zeta}) = \frac{\beta^3 |\hat{\phi}(\hat{\zeta})|}{\sum_{\hat{\eta}^* \neq \hat{\eta}} \beta^3 |\hat{\phi}(\hat{\eta}^*)|} = \frac{\beta^3 \hat{\phi}(\hat{\zeta}) \text{sgn}(\hat{\phi}(\hat{\zeta}))}{\sum_{\hat{\eta}^*} \beta^3 \hat{\phi}(\hat{\eta}^*) \Big|_{\hat{\phi}(\hat{\eta}^*) > 0} - \sum_{\hat{\eta}^*} \beta^3 \hat{\phi}(\hat{\eta}^*) \Big|_{\hat{\phi}(\hat{\eta}^*) < 0} - \beta^3 |\hat{\phi}(\hat{\eta})|}. \quad 15$$

In Eq. 15 the denominator is split into positive and negative components because the current scheme allows for the distribution function to be positive or negative.

By defining the number density of negative mass, \hat{n}_{neg} as:

$$\hat{n}_{neg} = \sum \beta^3 \hat{\phi}(\hat{\eta}^*) \Big|_{\hat{\phi}(\hat{\eta}^*) < 0} \quad 16$$

Eq. 15 can be re-written as:

$$P(\hat{\zeta} | \hat{\eta}) = \frac{\beta^3 \hat{\phi}(\hat{\zeta}) \text{sgn}(\hat{\phi}(\hat{\zeta}))}{\hat{n} - 2\hat{n}_{neg} - \beta^3 |\hat{\phi}(\hat{\eta})|}. \quad 17$$

Equation 17 is the probability of point $\hat{\zeta}$ being randomly selected to collide with $\hat{\eta}$. The expectation value of the depletion at $\hat{\zeta}$ as a result of being randomly selected is the product of the probability of being selected, the total number of random collision partners M_j , and the depletion, d/M_j , per collision partner:

$$\langle \Delta \hat{\phi}_{depl}(\hat{\zeta} | \hat{\eta}) \rangle = P(\hat{\zeta}) M_j \frac{d}{M_j}, \quad 18$$

where d is defined as:

$$d \equiv \frac{1}{2} \Delta t \hat{\phi}(\hat{\eta}) (\hat{n} - 2\hat{n}_{neg} - |\hat{\phi}(\hat{\eta})| \beta^3) \text{sgn}(\hat{\phi}(\hat{\zeta})). \quad 19$$

Substituting Eqs. 17 and 19 into 18 we obtain:

$$\langle \Delta \hat{\phi}_{depl}^{half}(\hat{\zeta} | \hat{\eta}) \rangle = \hat{\phi}(\hat{\zeta}) \text{sgn}(\hat{\phi}(\hat{\zeta})) \beta^3 \frac{1}{2} \Delta t \hat{\phi}(\hat{\eta}) \text{sgn}(\hat{\phi}(\hat{\zeta})) = \frac{1}{2} \Delta t \hat{\phi}(\hat{\eta}) \hat{\phi}(\hat{\zeta}) \beta^3 \quad 20$$

When summed over all velocities $\hat{\eta}$ the expectation for the depletion at $\hat{\xi}$ when chosen as a field point is:

$$\left\langle \Delta \phi_{depl}^{half}(\hat{\xi}) \right\rangle = \frac{1}{2} \Delta \hat{t} \hat{\phi}(\hat{\xi}) \sum_{\hat{\eta} \neq \hat{\xi}} \beta^3 \hat{\phi}(\hat{\eta}) \quad 21$$

Adding the contributions from 14 and 21, the expectation for the total depletion is identical to that given by Eq. 3.

To implement the above scheme into the computational code, Eq. 6 is used. For each test point, a set of M_j collision pairs are preferentially selected based on mass. The depletion, Eq. 6, is then evenly distributed among each collision pair. This is then repeated for all test points in velocity space.

REFERENCES

- [1] Bird, G.A., 1994, *Molecular Gas Dynamics and the Direct Simulation of Gas Flows*, Clarendon Press, Oxford.
- [2] Hash, D.B., Hassan, H.A., 1997, Two-Dimensional Coupling Issues of Hybrid DSMC/Navier-Stokes Solvers, AIAA paper: 97-2507.
- [3] Carlson, H.A., Roveda, R., Boyd, I.D., and Candler, G.V., 2004, A Hybrid CFD-DSMC Method of Modeling Continuum-Rarefied Flows, *Presented at the 42nd AIAA Aerospace Sciences Meeting*, Reno, NV, January 5-8 2004. AIAA paper: 2004-1180.
- [4] Nordsieck, A., and Hicks, B.L., 1967, Monte Carlo Evaluation of the Boltzmann Collision Integral, *Proc. 5th Intern. Symposium on Rarefied Gas Dynamics*, edited by C.L. Brundin, Academic Press, New York, pp. 695-710.
- [5] Yen, S.M., 1984, Numerical Solution of the Nonlinear Boltzmann Equation for Non-Equilibrium Gas Flow Problems, *Annu. Rev. Fluid Mech.*, **16**, 67.
- [6] Tan, Z., Varghese, P.L., 1994, The Δ - ε Method for the Boltzmann Equation, *J. Comput. Phys.*, **110**, 327.
- [7] Inamuro, T., and Sturtevant, B., 1990, Numerical Study of Discrete-Velocity Gases, *Phys. Fluids A*, **2**, 2196-2203.
- [8] Tcheremissine, F.G., 1969, A Method For Direct Numerical Integration of Boltzmann Equation, in *Numerical Method in the Theory of Gases*, Edited by V.P. Shidlovskii, Moscow: Comput Cent., USSR Acad. Sci. Transl. in NASA TT F-638, 43-63.
- [9] Tan, Z., Chen, Y.K., Varghese, P.L., Howell, J.L., 1989, New Numerical Strategy to Evaluate the Collision Integral of the Boltzmann Equation, in *Rarefied Gas Dynamics: Theoretical and Computational Techniques*, edited by E.P. Muntz, (AIAA, Washington, DC), 359.
- [10] Aristov, V.V., and Tcheremissine, F.G., 1985, The Kinetic Numerical Method for Rarefied and Continuum Gas Flows, in *Rarefied Gas Dynamics, Vol. 1*, edited by Belotserkovskii, et al., Plenum, New York, 269.
- [11] Bhatnagar, P.L., Gross, E.P., and Krook, M., 1954, Model for Collision Processes in Gases, I. Small Amplitude Processes in Charged and Neutral One-Component Systems, *Phys Rev.* **94**, 511-524.

- [12] Varghese, P.L., 2007, Arbitrary Post-Collision Velocities in a Discrete Velocity Scheme for the Boltzmann Equation, *in Rarefied Gas Dynamics: Proc of the 25th Intern. Symposium*, edited by M.S. Ivanov and A.K. Rebrov, Novosibirsk, Russia, 227-232.
- [13] Morris, A.B., Varghese, P.L., Goldstein, D.G., 2008, Improvement of a Discrete Velocity Boltzmann Equation Solver that Allows for Arbitrary Post-Collision Velocities”, *in Rarefied Gas Dynamics: Proceedings of the 26th International Symposium*, Kyoto, Japan.
- [14] Tcheremissine, F.G., 2005, Direct Numerical Solution of the Boltzmann Equation, *in Rarefied Gas Dynamics, AIP, Conference Proceedings*, NY, edited by M. Capitelli, **762**, 677-685
- [15] Popov, S.P., Tcheremissine, F.G., 1999, A Conservative Method for Solving the Boltzmann Equation with Centrally Symmetric Interaction Potentials, *Comput. Math. And Math. Phys.*, **39**, 156.
- [16] Tcheremissine, F.G., 2006, Solution to the Boltzmann Kinetic Equation for High-Speed Flows, *Comput. Math. And Math. Phys.*, **46**, 315.
- [17] Kolobov, V.I., Arslanbekov, R.R., Aristov, V.V., Frolova, A.A., and Zabelokm, S.A., 2007, Unified Solver for Rarefied and Continuum Flows with Adaptive Mesh Algorithm Refinement, *Journal of Comp. Phys.*, **223**, 589-608.
- [18] Bobylev, A.V., 1976, *Soviet Phys. Dokl.*, **20**, 822-824.
- [19] Krook, M., and Wu, T.T., 1977, *Phys. Fluid*, **20**, 1589-1595
- [20] Aristov, V.V., Tcheremissine, F.G., 1982, Shock Wave Structure in Monatomic Gas at Power Potentials, *Fluid Dynamics*, **2**, 179-183.
- [21] Ohwada T., 1993, Structure of Normal Shock Waves on the Basis of the Boltzmann Equation for Hard-Sphere Molecules, *Phys. Fluids A5*, 217-234.
- [22] Vincenti, W.G., Kruger, C.H., 1965, *Introduction to Physical Gas Dynamics*, Krieger, Florida.
- [23] Lennard-Jones, J. E., 1931, *Cohesion. Proceedings of the Physical Society*, **43**, 461-482.
- [24] Bird, G.A., 1981, Monte-Carlo Simulation in an Engineering Context, *Progr. Astro. Aero.*, **74**, 239-255.
- [25] Koura, K., and Matsumoto, H., 1991, Variable Soft Sphere Molecular Model for Inverse-Power-Law or Lennard-Jones Potential, *Phys. Fluids A 3*, 2459-2465.

- [26] Bird, G.A., 1983, Definition of mean free path for real gases, *Phys. Fluids*, **26**(11).
- [27] Bird, G.A. 1980, Monte-Carlo Simulation In An Engineering Context, *Rarefied Gas Dynamics: Proceedings of the 12th International Symposium*, July 7th-11th, Charlottesville, Va.
- [28] Goldstein, D., 1990, Investigations of a Discrete Gas, California Institute of Technology, Pasadena, CA.
- [29] Heintz, A., Kowalczyk, P., and Grzhibovskis, R., 2008, Fast Numerical Method for the Boltzmann Equation on Non-Uniform Grids, *Journal of Comp Phys*, **227**, 6681-6695.

VITA

Aaron Benjamin Morris was born in Dayton, Ohio on August 28th, 1984, the son of Rosemary and John Morris. After attending high school at Shaker High School in Latham, New York he continued his education at Rensselaer Polytechnic Institute from the fall of 2002 through the spring of 2006. In 2006, he received his Bachelor of Science degree in mechanical engineering from Rensselaer Polytechnic Institute. After graduating from Rensselaer Polytechnic Institute, he attended the University of Texas at Austin in August of 2006 to pursue his Masters degree and PhD in aerospace engineering.